Oncoslice: A Microfluidic Platform for Personalized Cancer Care and Drug Development

Adan David Rodriguez Arizpe

A thesis

submitted in partial fulfillment of the

requirements for the degree of

Master of Science in Bioengineering

University of Washington

2018

Committee:

Prof. Albert Folch, Chair

Prof. Barry Lutz

Program Authorized to Offer Degree:

Bioengineering

University of Washington

Abstract

Oncoslice: A Microfluidic Platform for Personalized Cancer Care and Drug Development

Adan David Rodriguez Arizpe

Chair of the Supervisory Committee:

Prof. Albert Folch

Department of Bioengineering

Improving efficacy, minimizing the adverse side effects of drugs, and overcoming acquired resistance to drug treatment have been major goals and emphases in cancer therapy. Existing models of drug activity (based on tumor cells in culture or animal models) cannot accurately predict how drugs would act in individual patients. Presonalized medicine has received considerable attention and enthusiasm as it has potential to offer new therapeutic measures based on tailored therapies for individual patients. Personalized approaches could lower treatment toxicity, improve patient's quality of life, and, most importantly, reduce mortality. Prof. Folch's lab developed Oncoslice, a platform has the potential to allow for identifying the subset of therapies of greatest potential to individual patients, on a timescale rapid enough to guide therapeutic decision-making. This new method would allow for testing treatment efficacy on the patient's own tumor tissue in a timeline that allows for the results to influence a patient's therapeutic strategy. However, the platform was fabricated with conventional soft-lithography techniques, which are not readily translatable for mass manufacturing. Here we present a redesigned architecture of Oncoslice and new manufacturing techniques that will facilitate its fabrication on the larger scale necessary for clinical use. We shifted our focus to CO_2 laser micromachining as the main fabrication technique and we were able to develop a new fabrication protocol with rapid turnaround time, low operational costs, mask/cast-less processes, and agile design processing. We focused on poly (methyl methacrylate) (PMMA) as the fabrication material of the platform due to its biocompatibility, low-cost, and optical properties. This thesis reports a detailed description of the complete fabrication process including CO_2 laser optimization, post-processing, and solvent bonding techniques for assembly. Moreover, we also present alternative bonding procedures commonly utilized for rapid-prototyping, such as indirect transfer adhesive bonding and lamination. Finally, we demonstrate the functionality of the platform through a series of characterization experiments and illustrate its potential through a set of biological experiments utilizing glioblastoma multiforme xenografts and human colorectal cancer biopsies.

Acknowledgements

I would first like to express my deep appreciation and gratitude to my advisor, Prof. Albert Folch, for the patient guidance and mentorship he provided me to complete each task of this project. The door to Prof. Folch office was always open for me whenever I faced difficult challenges during my research. Albert consistently allowed this project to be my own work, but he always steered me in the right direction and kept me motivated to rise from all the challenges associated with this project.

I would also like to thank Dr. Lisa Horowitz, Dr. Nirveek Bhattacharjee, and Kurt Castro for their invaluable contributions to this work. Similarly, I would like to show my appreciation to all the other members in the lab for their support and collaboration. I would also like to acknowledge the financial support through research assistantship from Prof. Albert Folch and the University of Washington. I would also like to acknowledge the financial support from the Consejo Nacional de Ciencia y Tecnología (Mexico). My research would not have been possible without their support.

Finally, I must express my very profound gratitude to my parents and girlfriend for providing me with unfailing support and continuous encouragement throughout my years of study and through the process of researching and writing this thesis. Thank you.

Table of Contents

List of figures

List of tables

1. Introduction

Cancer has a significant impact on society in the United States and across the world. In 2017, an estimated 1.7M new cancer cases and 600,000 cancer deaths were projected to occur in the United States [1], [2].There is a critical unmet need to develop and tailor chemotherapies to individual cancer patients. Personalized methodologies have the potential to lower treatment toxicity, improve patients' quality of life, and ultimately reduce mortality. The National Cancer Institute (NCI) has identified that "current methods to assess potential cancer treatments are cumbersome, expensive, and often inaccurate" and has issued the challenge "to develop methods to rapidly test interventions for cancer treatment or prevention"[3]. The NCI describes numerous challenges, among them limited patient population and complicated selection strategies, extensive clinical validation of a target, drug class, or mechanism of action, and complex clinical trials. All of these challenges have a direct impact on the costs behind safe and effective drug development.

The average cost of developing a new cancer drug is now more than $700 million [4]–[6]. Most pharmaceutical drugs in clinical development phase never make it to market; in a recent report, 84% of the failures were due to a lack of efficacy (56%) or to safety issues (28%), with almost 30% being cancer drugs [7], [8]. One of the main causes of this expensive gridlock is that pre-clinical animal tests – which are required by the FDA – do not accurately predict toxic doses and drug metabolism observed in humans [9]. Clearly, there is an urgent need for better test assays based on human tissue which would more closely mimic patient disease and predict clinical outcomes better than 2D cell culture systems and animal models. The NCI Provocative Questions in Cancer states that "If systems can be developed that accurately predict drug responses in human, advances in drug treatment or prevention would be dramatically streamlined, and time frames for drug development shortened considerably"[3].

Precision oncology is described as the matching of the most accurate and effective treatments with the individual cancer patient [10]. The demand for new diagnostic tools has been driven by precision therapies and the motivation to advance personalized medicince. In particular, the use of biopsies and patient-derived xenograft (PDX) models has received substantial attention from researchers and clinicians. For precision diagnosis, having new biopsy-based diagnostic platforms is crucial because these type of assays can gather information from patients in a manner that is minimally invasive. For precision therapy, testing drugs in a paradigm like the PDX model is beneficial because this model can be used to represent tumors of patients before drugs are prescribed [10].

In the last decade, investigators have increasingly utilized live tumor tissue to better replicate tumor physiology in pharmacodynamic and cancer biology experiments. As evidence mounts that the surrounding stromal cells play key roles in tumorigenesis and tumor progression [11], it has become clear that dissociated tumor cell culture models cannot faithfully replicate the spatiotemporal complexity of tumor biology [12]. Four approaches stand out, listed by increasing physiological relevance and decreasing throughput: 1) "tumor organoids" (small spheroids

formed from patient-derived, dissociated cells [13]–[18]), a model that can create cell-cell and cell-matrix 3-D interactions that more closely resemble in-vivo interactions and has been used for high-throughput drug screening assays that can be predictive of the patient's responses [19]; 2) "micro-dissected tumor tissues" [20] based on the submillimeter mechanical fragmentation of biopsies, an approach that suffers from reduced tissue viability; 3) the "organotypic" tissue culture technique [21] (based on culturing tissue slices atop a porous membrane support) has been used for many decades and recently applied to cancer with great success [14-17], although testing large numbers of drugs remains difficult; and 4) implantable needle devices [22], [23] that deliver small doses of drugs to the tumor in vivo in a point-source diffusive fashion. In each of these techniques higher throughput (and thus lower cost) is obtained at the expense of less physiological relevance, it is still unclear which techniques will be more useful for preclinical testing of drugs and which will become a clinical standard.

To improve the shortcomings of the current live tumor tissue approaches, the Folch lab presented [24] and patented [25] a microfluidic platform, termed Oncoslice (Fig. 1). Oncoslice permits regioselective delivery of drugs with spatiotemporal control on live tissue cultures. The platform was a 96-well plate-based microfluidic device fabricated using traditional soft-lithography techniques, polyIdimethylsiloxane (PDMS) replicas, oxygen plasma for PDMS–PDMS and PDMS–glass bonding, and silane coupling for PDMS-Polystyrene bonding. The device was assembled from 4 parts including a modified bottomless 96-well plate, a PDMS layer containing through-holes, a PDMS channel network layer, and a thin microfluidic chip. The microfluidic platform demonstrated two key features that overcome current limitiations of high-throughout drug screening on intact tissues; it showed the capability to couple organotypic slice culture with a microfluidic drug delivery device and the adaptation of this approach to a familiar multi-well plate format, enabling multiplexed fluid routing and facilitiating tissue handling and imaging for assessing tissue drug response patterns. Furthermore, the publication served to illustrate how the platform has a great potential to improve on existing models for screening chemothrapeutic drug activity and to generate response data in a time frame that could guide decision-making for the initial phases of cancer therapy.

The novelty of Oncoslice showed great promise on collaborating towards the needs stated by NCI by improving the assays for drug development and, ultimately, to open an avenue to personalized medicine for cancer patients. However, the complex and laborious fabrication process of the platform became a barrier as the lab tried to continue to show its potential. The overarching goal of my Masters research project was to to improve the design, fabrication, and manufacturability of Oncoslice. Through a complete redesign of the microfluidic architecture of the platform, the incorporation of biocompatible thermoplastics, reliable fabrication techniques, and digitial manufacturing we were able to develop a protocol that will hopefully enable Oncoslice to serve as a tool for drug development and personalized medicine.

1.2 Background - Oncoslice device original design

The first design was based on a 96-well plate microfluidic device. The platform was fabricated using soft-lithography, ploy(dimethylsiloxane)(PDMS) replicas, oxygen plasma for PDMS-PDMS and PDMS-glass bonding, and silane coupling for PDMS bonding to polystyrene. The device was assembled from 4 parts including a modified bottomless 96-well plate, a PDMS layer containing through-holes, a PDMS channel network layer, and a thin PDMS microfluidic chip (Fig. 1a).

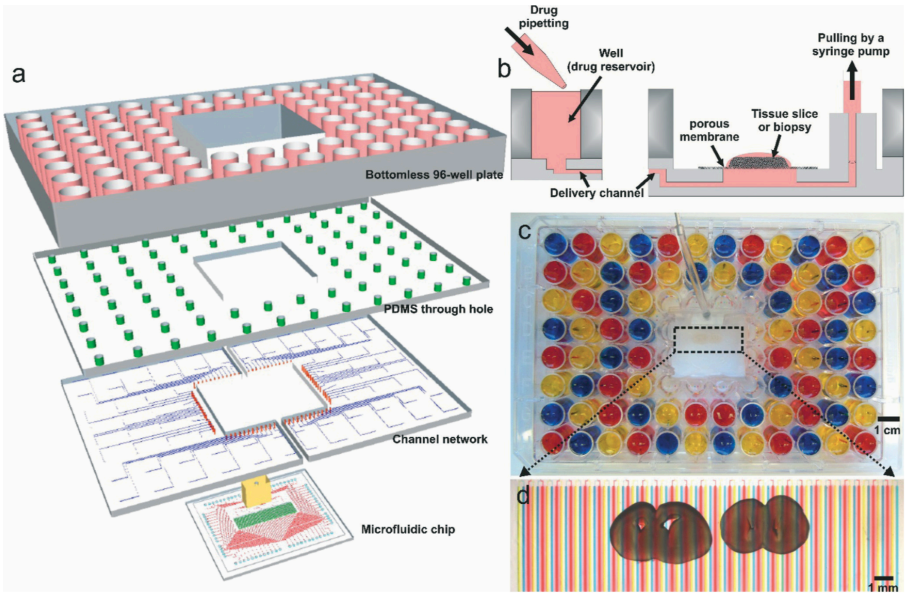

Figure 1 Oncoslice original device design. (a) Layer-by-layer schematic view of the device. The device includes (from top to bottom) a modified bottomless 96-well plate featuring 80 inlet wells after the central 16 wells have been removed; a PDMS layer containing through-holes layer; a PDMS microchannel network layer; and the microfluidic chip (where the porous membrane with the tissue is placed). (b) Cross-sectional schematic of the device. The device is operated by gravity flow and the total flow rate is driven by a syringe pump through a common outlet: one syringe pump is able to control flow across all 80 fluidic streams. Tissue slices are cultured on a PTFE porous membrane. The wet membrane seals the open microchannels by capillarity, which allows for fluidic stream transport of culture medium to tissue. (c) Micrograph of the microfluidic platform loaded with three dyes (yellow, blue and red) in sequence to generate an alternating pattern of yellow, blue and red microchannels across the perfusion membrane. (d) Micrograph of the tissue culture area after loading the platform shown in (c) with a porous membrane that has two mouse brain slices attached.

The bottomless polystyrene 96-well plate was modified to fit a square by removing a 4 x 4 well area, leaving 80 inputs. The PDMS through-hole layer contained 3 mm holes and a central square which were made manually to fit the modified 96-well plate. The PDMS channel network consisted of two separate PDMS molds that assembled to make a complete channel network to distribute the fluids from the well inlets to the tissue. The microfluidic chip had 80 parallel open channels which sat beneath a PTFE membrane. Each open channel was 8 mm long and 100 μm wide. The flow rates were equilibrated by adjusting the microchannel resistances. The equivalent resistances of this design had ~15% variability between each other.

The assembled platform was treated with oxygen plasma for bonding, sterilization, and hydrophilization prior to use. After plasma treatment the device is filled with PBS or culture medium and it was ready to use after covering the open channels with a PTFE membrane and

activating flow by applying suction with a syringe pump (Fig. 1b). Tissue slices could be transferred from the porous membrane well insert by first cutting the PTFE membrane and placing it on top of the open microchannels of the device. The first design offered a total of 80 parallel open channels that were connected to the reservoirs in the well plate (Fig. 1c&d). The well reservoirs could then be filled with either drug or buffer, depending on the desired spacing.

This first design had the advantage of having 80 delivery channels into the culture chamber. Assuming that the user would space the chemicals of interest from each other, the platform would allow for the delivery of 27 different compounds. The micron-level dimensions of the first design were only achievable through conventional soft-lithography. Although soft-lithography is still widely used in laboratories that focus on developing similar and more sophisticated microfluidic platforms, it tends to hinder the ability to transition to a clinical setting that requires a larger scale of device manufacturing. In the case of Oncoslice, the labor behind its fabrication and manufacturing limited its potential to move forward to serving its purpose outside a laboratory.

The yield and reproducibility of the device was one of the biggest issues; in a normal day of fabrication the probability of having a 100% functional device was about 10%. The main reason of such low fabrication throughput was related to the complexity of the alignment of the different PDMS layers during assembly. The assembly of the platform had a very critical alignment step; the alignment of the channel layers with the microfluidic chip. This step had an alignment tolerance of ~150 μm, resulting on a nearly impossible task to align 80 different micron-sized holes with each other.

The second issue of most importance was the time of fabrication. The time of fabrication, only including the fabrication of each layer and the assembly of the platform, was about one day. This time measurement did not include the time required to develop the silicon wafer molds used for each PDMS layer, the time it took to modify the 96-well plate, and the time it took between each plasma treatment. Considering every step (for both soft-lithography and photolithography) it took about 4 days to fabricate a single device.

The third issue was the complications behind prototyping. As with any other device, there were problems that were associated with functionality, some of them related to fluid transport within the channel network. In a microfluidic platform with characteristics similar to Oncoslice, every channel has to have the same resistance for uniform flow across the device. To achieve this, slight modifications have to be made as part of the prototyping process. Such adjustments can only be solved by redesigning the CAD drawings, sending them for mask development, and remaking the silicon molds through SU-8 photolithography. This meant that a slight modification of the microfluidic architecture of the platform could take up to 4 weeks.

Apart from these three challenges, there were other fundamental challenges that directly affected the functionality and manufacturability of the device. The first design of the platform was made of two very different materials: PDMS and polystyrene. Due to the difference in material properties of these two polymers, the chemical bonding process during the assembly

was not trivial and it often led to leaks. Apart from having two different materials, there were other problems related to the main outlet and the overall toughness of the device. The outlet was very fragile, and it often tore after continuous handling. Similarly, the glass piece could easily break if the platform was placed on a rough surface or if it accidentally fell to the ground. Having all of these challenges in mind we sought to begin a complete redesign of the platform and to establish an enhanced fabrication protocol.

2. First major design modifications and motivation for transition to digital manufacturing technologies

The first idea was to modify the dimensions of the device to facilitate its assembly. Knowing that the reliability and reproducibility were hindered by the difficulties that came with alignment, modifying the overall architecture of the device was the first improvement (Table 1).

Table 1 First major design modifications

Modifications	Original Design	First Redesign
Number of Channels	80	40
Channel Width	100 μm	200 μm
Drug Spacing (edge-edge)	650 μm	850 μm
Variance in Channel Resistance	~15%	~5%
Alignment Tolerance	150 μm	750 μm

The major modification was a reduction on the number of channels; we decided to decrease the number of channels from 80 to 40 (Fig. 2). This alteration allowed us to double the width of each channel and connection. In the first design the widths varied from ~50 μm to ~200μm. Such variation was a result of their different lengths. The variation in length and width allowed for a balancing of resistances across all the channels. After employing the first modification, each channel now had the same length and a varying width ranging from ~100 μm to ~400μm. Similarly, the width of the open channels in the culture chamber changed from 100 μm to 200 μm. During this size alteration process, we were also able to reduce the variance in channel to channel resistances from ~15% to ~5%. The limitation on the previous design was space, having greater space allowed for major changes in length to compensate for differences in resistances.

As shown in Figures 2c and 2d, the spacing in the open lanes also changed. With the first design, the platform allowed for a total of 27 drug lanes spaced out with 53 buffer lanes (2 buffer channels in between every drug channel). The spacing between each drug, from the edge of the first drug channel to the edge of the next one was 650 μm. After the modification, this spacing changed to 850 μm. Similarly, the number of drug and buffer channels were both reduced to 20. Greater spacing between drug channels resulted in less risk for cross-talk between two different compounds.

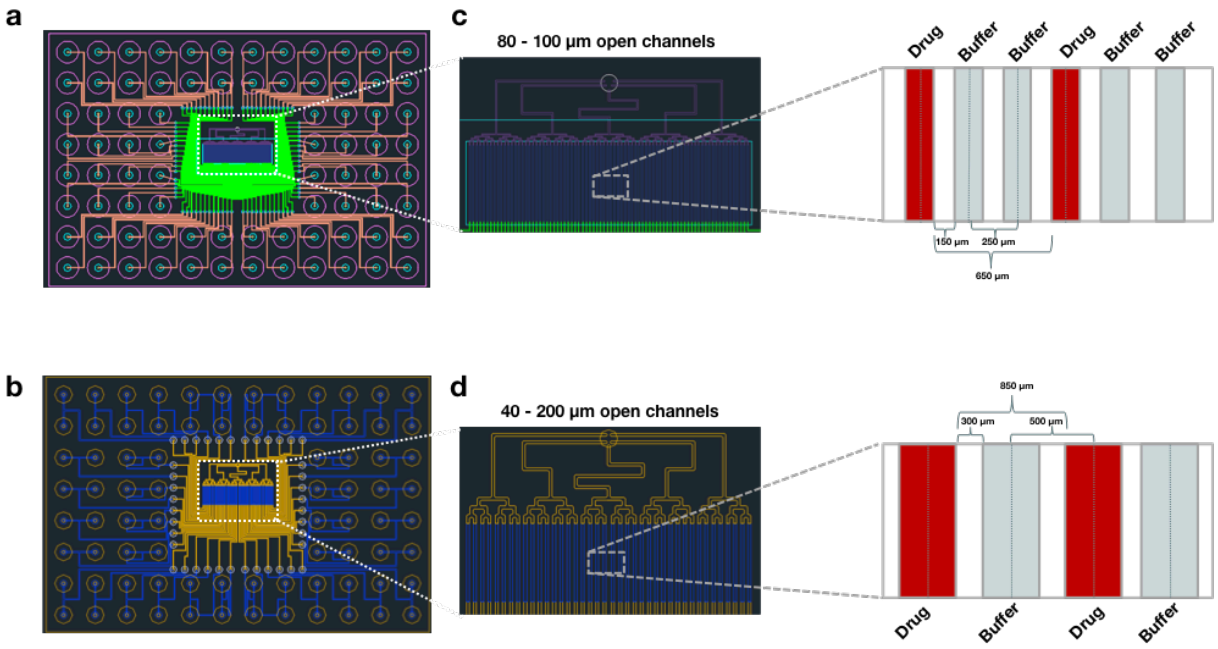

Figure 2 First major design modifications. a) Original platform architecture with 80 delivery channels. b) First major design modification reducing the number of delivery channels from 80 to 40. c) Open channel dimensions, spacing, and drug arrangement. d) Resulting open channel dimensions, spacing, and drug arrangement after size modification.

With a reduced number of channels covering the overall architecture, we were also able to modify the size of the vias connecting the channel layer to the microfluidic chip layer. In the first design, the connectors in the channel network layer had a diameter of 500 µm while the connectors in the microfluidic chip layer had a diameter of 800 µm. Such dimensions resulted in an alignment tolerance of 150 µm, making the assembly of the device very challenging and problematic. As a result, the dimensions of the connectors of the microfluidic chip were modified to 2mm. This modification increased the alignment tolerance to 750 µm.

2.1 Balancing equivalent resistances

During the first major design modification, the equivalent resistance of each channel was accounted for in order to reduce variability of resistance across the platform. First a calculation of the equivalent resistance across each channel in the original design was performed. These calculations were made using the equation to calculate pressure drop along rectangular microchannels; accurate within 0.26% for any rectangular channel that has W/H less than 1, provided that the Reynolds number (Re) is below y1000 [26]:

$$\Delta P = QR \qquad (1)$$

$$\Delta P = \frac{\alpha \mu Q L}{W H^3} \qquad (2)$$

In a rectangular channel in which there are no bubbles or obstructions present, the laminar flow of a single liquid phase through the channel approximately follows eqn. (2), where L (m) is the length of the channel, W (m) is the width of the channel, H (m) is the height of the channel, μ is the viscosity of the liquid, and α is a dimensionless parameter that depends on aspect ratio, W/H, defined as:

$$\alpha = 12\left[1 - \frac{192\mathrm{WH}}{\pi^5 \mathrm{W}}\tanh\left(\frac{\pi \mathrm{W}}{2\mathrm{H}}\right)\right]^{-1} \quad (3)$$

Therefore, in order to calculate the equivalent resistance, we can combine equations (1) and (2) to obtain:

$$\mathrm{R} = \frac{\alpha \mu \mathrm{QL}}{\mathrm{WH}^3} \quad (4)$$

Similarly, since the height, the flow rate, and the viscosity in the system were kept constant among every channel, we can observe how the resistance is directly proportional to the length to width ratio:

$$\mathrm{R} \propto \frac{\mathrm{L}}{\mathrm{W}} \quad (5)$$

After measuring the length and width of each channel and calculating the respective value of α, the equivalent resistance across the channels in the original device had a 15% deviation from the mean. Such problem was resolved by adjusting the width and length to accomplish an equal equivalent resistance across every channel. By leveraging the advantage of having greater space, adjusting the length of each channel correspondingly resulted in a ~5% deviation from the mean across the platform with the new design.

2.2 Time of fabrication through soft-lithography

One of the main objectives of this project is to develop a fabrication protocol that is amenable for mass manufacturing. Therefore, each fabrication step was timed and grouped into the categories shown in Table 2. After timing each step of the process repeatedly, the total time of fabrication per device was about 445 minutes or 7.4 hours. With the time required to produce one device and assuming no errors were made, only allowed for the fabrication of one device per day.

Table 2 Total time of fabrication per device after photolithography

Part / Process	Time (min)
Modified 96-well plate + PDMS Hole Layer	130
Channel Layer (soft lithography)	140
Chip Layer (soft lithography)	130
Alignment and Bonding	45
Total Time	445 (~7.4 hours)

2.3 Motivation for transition to digital manufacturing

Even after the first major redesign of the platform, other problems related to fabrication were still present and the protocol was not 100% reliable; the yield was still very low. Some of the problems were related to the differences in the properties of each material used in the device, specifically during bonding. For example, the chemical bonding between polystyrene and poly (methyl methacrylate) (PMMA) was not always perfect and resulted in leakage. Other problems were related to the outlet made out of PDMS and to the fragility of the glass slide used for the microfluidic chip layer. A vast number of devices failed due to at least one of these problems or a combination thereof. Another important factor is that the time calculation shown above was only based on the fabrication process after photolithography. Wafer development for this device took approximately 4 weeks to complete for every iteration.

After considering all the issues and observing the new dimensions of the platform, the solution clearly pointed towards digital manufacturing. Digital manufacturing would increase the reliability of our fabrication protocol, reduce the production time per device, and allow for rapid prototyping. We explored the possibility of using AutoCAD in conjugation with CNC micromachining and CO_2 laser engraving technologies. Due to the ease of access and the capabilities of CO_2 laser engraving, we decided to move forward with this technology.

3. Current device and fabrication protocol

The current fabrication protocol was a result of numerous attempts to solve each of the problems outlined in the previous sections. Several processes and methodologies were attempted, all of which are outlined in the next chapter of the thesis. After experimenting with different fabrication approaches, we were able to formulate a protocol that would provide the necessary reliability and reproducibility for manufacturing on a larger scale. The finished protocol has four major parts: an AutoCAD design of each of the device components, fabrication of each component using a CO_2 laser, post-processing, and solvent bonding for device assembly.

With an AutoCAD design, we now have the advantage of rapid prototyping to solve any future problems related to device functionality or for additional design improvements. The fabrication of each component is now made with the Universal Systems Laser VLS 3.60 and ILS 12.150D machines. One of the major challenges of the transition to CO_2 laser was the optimization of the machine parameters for each device component. After careful assessment of the properties of the machine and its laser, we were able to determine the optimal parameters for each of the components of the device. A detailed study of the parameters that led us to the optimal setting is also presented on the next chapter. Finally, to solve all the problems related to material compatibility the platform is now made up of only PMMA. We chose PMMA due to its biocompatible and optical properties, low cost, and compatibility with digital manufacturing techniques. Having only one material solved many of the problems related to layer bonding and device assembly. The assembly of the platform is now accomplished by a combination of thermal fusion bonding using chloroform and solvent welding with methylene chloride.

3.1 Device overview and operation

As shown in Figure 3a, the platform now consists of 5 components (from top to bottom): a lid that allows air flow, a 40-well plate with a central culture chamber, a microfluidic channel network layer, a sealing layer for the channel network, and the plate bottom. The assembled platform is treated with oxygen plasma for sterilization and hydrophilization prior to use. After plasma treatment the device is filled with PBS or culture medium and it is ready to use after covering the open channels with a PTFE membrane and activating flow by applying suction with a syringe pump (Fig. 3b). Live tumor slices or biopsies can be transferred from the porous membrane well insert by first cutting the PTFE membrane and placing it on top of the open microchannels of the device (Fig.3c). The platform allows for live tissue culture and high-throughput delivery of up to 40 solutions.

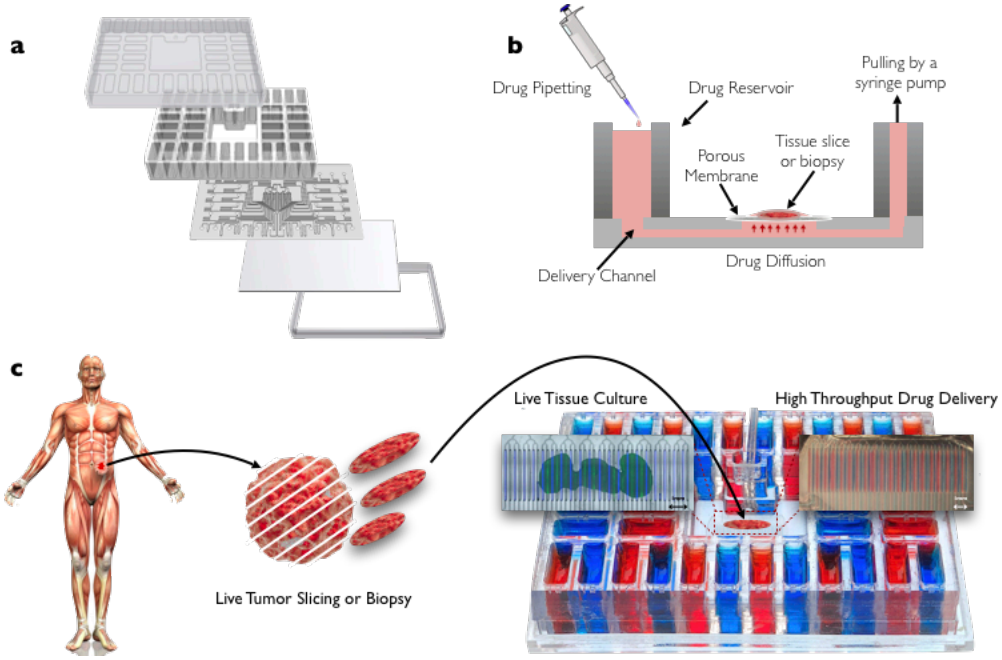

Figure 3 Microfluidic device design. (a) Exploded schematic of the platform showing a PMMA bottomless plate with 40 inlet wells and a laser-cut 300µm channel network layer. (b) Cross-sectional schematic of the device. The device is operated by gravity flow and the total flow rate is driven by a syringe pump through a common outlet: one syringe pump is able to control flow across all 40 fluidic streams. Tissue slices are cultured on a PTFE porous membrane. The wet membrane seals the open microchannels by capillarity, which allows for fluidic stream transport of culture medium to tissue. (c) Overview of proposed application and device functionality. Micrographs of a mouse glioma tumor slice exposed to two different cell nuclear binding agents (Hoechst, blue, and Sytox Green, green) through the alternating streams and high throughput delivery demonstration with two alternating dyes.

3.2 Overview of device fabrication and assembly

The overall fabrication of the device consists of laser cutting/engraving each of the components of the microfluidic platform, post-processing, thermal fusion bonding using chloroform, assembly through solvent bonding with methylene chloride, and accessory installation (Fig. 4). To laser cut

each of the components we used two different machines, the Universal Systems Laser VLS 3.60 and ILS 12.150D. The 40 well plate is made using the ILS 12.150D due to its higher power capacity, while the rest of the components are made with the VLS 3.60. The laser usually leaves residual PMMA and debris, requiring for several processing steps. Imperfections and debris are first removed with deionized (DI) water and isopropanol alcohol (IPA) sonication. After cleaning and drying each layer is treated with chloroform for smoothening. Then the channel network is sealed through a thermal fusion bonding step. The final bonding step, consists of attaching the channel network layer to the 40-well plate and it is accomplished through solvent welding with methylene chloride. The last step is the installation of the outlet and other accessories, like the top and bottom. All of the steps mentioned in this overview are explained in detail on the next sections within this chapter.

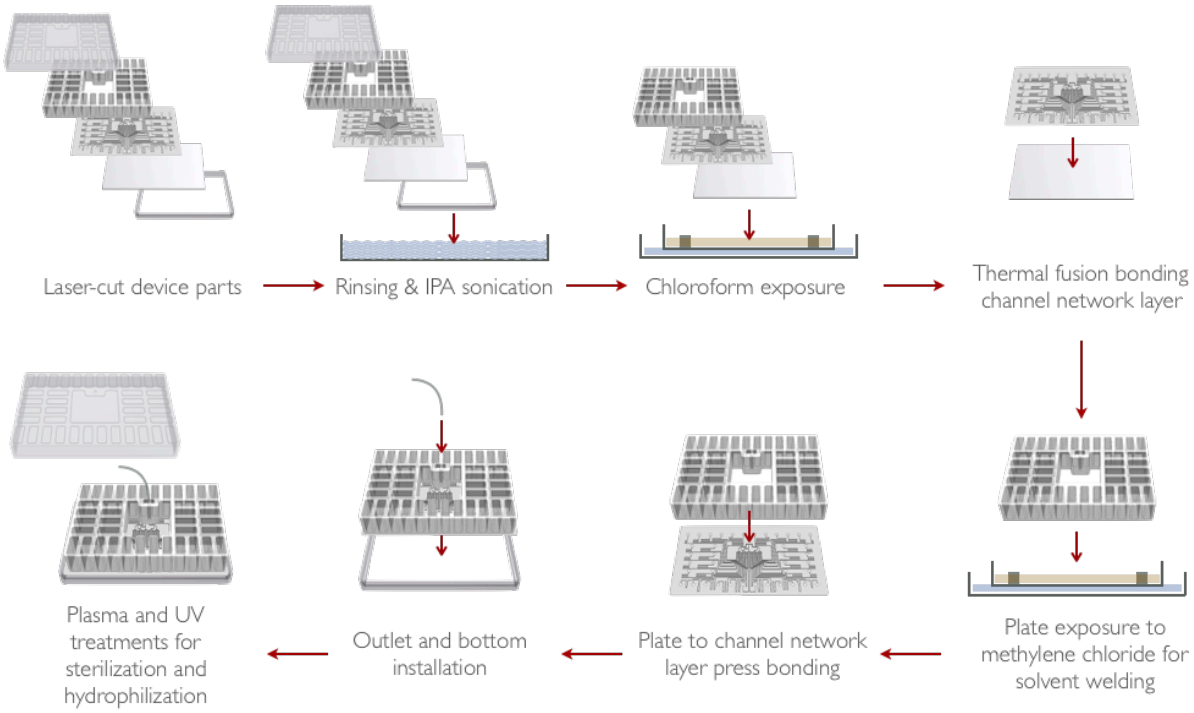

Figure 4 General overview of device fabrication protocol

3.3 Detailed channel network fabrication and assembly

The fabrication of the channel network required vast investigation on each of the steps shown in Figure 5. The first step consisted on determining the optimal laser settings to engrave the microfluidic channel network with the desired dimensions. The settings and resulting channel dimensions are thoroughly explained on the next chapter of this manuscript. The channel network is engraved on a clear 300 μm PMMA sheet. Similarly, a 125 μm PMMA with the outer dimensions of the channel network is made to seal the open channels. After cutting, the layers are rinsed with water and sonicated in IPA to remove debris. Once the layers are clean, they are exposed to chloroform for surface smoothening and prepared for thermal fusion bonding; the details behind the mechanism of action of chloroform are also explained in detail on the next

chapter. First, the channel network is exposed to chloroform vapor for 4 minutes and set to a side after exposure. Then, the sealing layer is exposed to chloroform vapor for 2 minutes. Immediately after exposure, the sealing layer is hand-pressed to the channel network, the complex is placed between two PDMS slabs to ensure homogenous pressing and transferred to a Carver Inc. 4126 Heat Press. The channel network is sealed by pressing at 160 psi and 60 °C for 10 minutes. Once the channel network is sealed, the functionality of each of the channels is evaluated under the microscope by filling their inlets with 50 µL of food coloring dye. Finally, if the channel network passes the leak and functionality test, it is prepared for the final assembly to the 40-well plate.

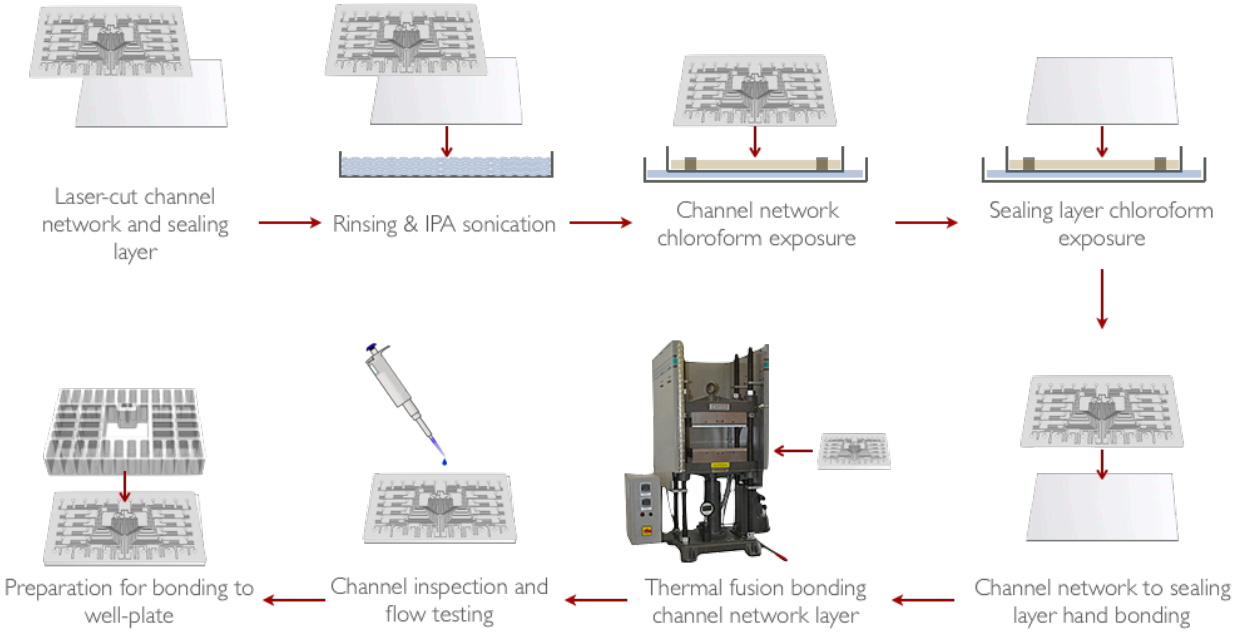

Figure 5 Channel network layer fabrication and bonding process

3.4 Detailed 40-well plate fabrication and assembly

The 40 well-plate is made by laser cutting through a 0.75" PMMA block using the ILS 12.150D laser system. Due to the high power required to cut through the PMMA block, we encountered burning, melting, and warping of the final piece. First, to prevent melting and burning of the material, a 0.1" PMMA was placed below the PMMA block on the cutting bed, which allows for greater air circulation. Second, to prevent warping, the laser-cut well plate is immediately placed between two cold metal pieces until it reaches room temperature. The well plate is then placed in the hydraulic press at ~1000 psi and 110 °C for 20 minutes. Then, it is left in the heat press until cool down for another 20 minutes. This ensures that the well plate is smooth and homogenous in its surface; two conditions that are critical for assembly.

After the well-plate is cut and flattened, it is rinsed with water and sonicated with IPA to remove excess debris. Once the plate is clean, it is exposed to chloroform vapor for 30 minutes to further smoothen its surface in preparation for bonding to the channel network. The smoothened plate

is then placed in a methylene chloride bath for 15 seconds and directly hand pressed to the previously made channel network layer. The bonded pieces are then placed in between two PDMS slabs to ensure homogenous pressing and pressed in the hydraulic press at 180 psi for 5 minutes. Finally, the bonded pieces are assembled to the plate bottom.

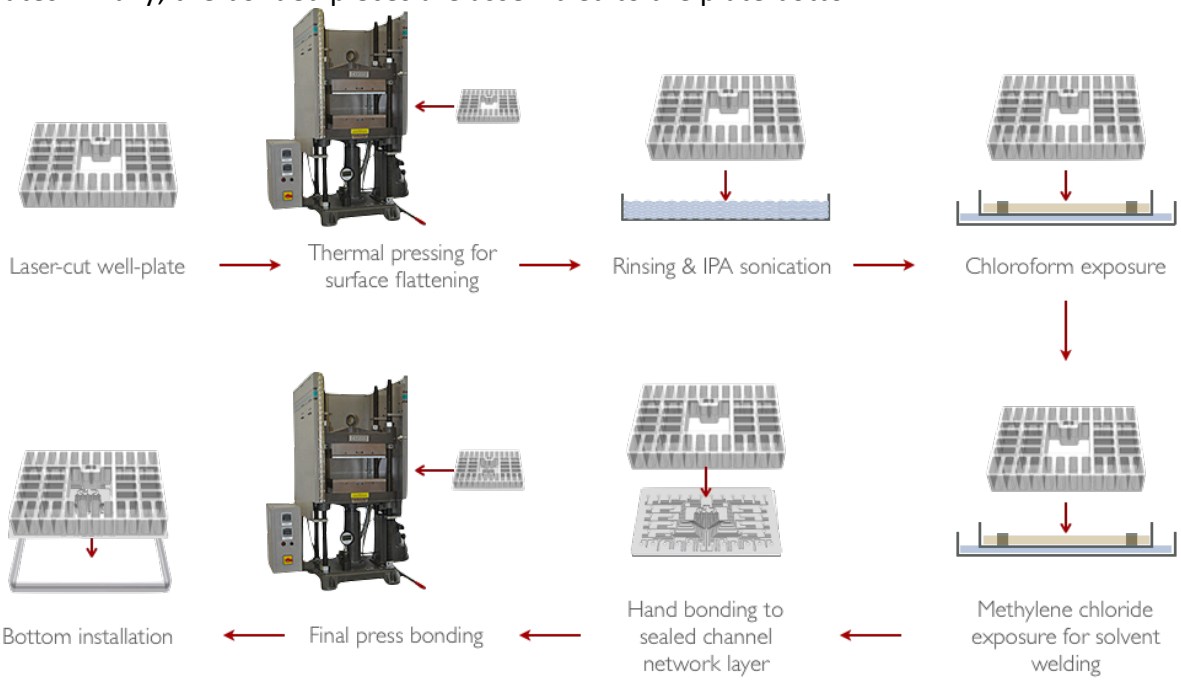

Figure 6 Well plate fabrication and bonding to channel network layer

3.5 Total fabrication time

After a complete transition to digital manufacturing, the total time per device has been successfully reduced to ~140 minutes. Apart from the reduction in time, we were also able to develop a reliable and reproducible fabrication protocol that can be easily followed by any person in the lab without rigorous training.

As shown in Table 3, fabricating and processing the 40 well-plate is currently taking about 50% of the total time of fabrication. The time required to flatten and smoothen the surface of the well-plate can be reduced by further assessing both of the steps. Currently, the well-plate is flattened with and without heat for 20 minutes respectively. A methodic experiment can be performed to investigate the possibility of reducing the pressing time accordingly. Additionally, the plate is exposed to chloroform for 30 minutes to ensure a smooth surface for a flawless bond with the channel network layer. Similarly, a time-lapse experiment can demonstrate the required exposure time and, most likely, reduce it in the final protocol. We are expecting to further reduce the fabrication time to 100 minutes by reducing the time of both of these steps by 50%.

In addition of being reliable and reproducible, the fabrication protocol is amenable for rapid-prototyping and for larger scale manufacturing. Design changes can be made and instantly tested, which leads to a continuous improvement of the platform. It is important to note that the time

noted in this table is assuming only one device is being fabricated. Ideally, on a manufacturing line, devices would be fabricated in line and the time in each of these steps would be reduced considerably.

Table 3 Total fabrication time with digital manufacturing techniques

Step	Time (min)
	Laser Cutting
Lid	3
40-Well Plate	20
Channel Network	10
Sealing Layer	0.2
Bottom	2
	Processing
Rinsing and IPA Sonication (all components)	5
40-Well plate press-flattening	40
40-Well plate chloroform exposure	30
Channel network chloroform exposure	4
Sealing layer chloroform exposure	2
40-Well plate methylene chloride exposure	0.25
	Assembly
Channel network to sealing layer bonding	10
40-well plate to channel network bonding	5
Outlet	5
Lid	2
Bottom	2
Total time	140.45

4. Incorporation of reliable fabrication techniques and digital manufacturing technologies

The development of a reliable and reproducible fabrication protocol required an extensive investigation of digital manufacturing, processing, and bonding techniques. Similarly, the microfluidic architecture and overall design of the platform had to be modified for an optimal performance with the chosen fabrication methods. Specifically, the microfluidic channel network underwent 4 major iterations that led towards the current design; a design that is optimal for digital manufacturing with CO_2 laser technologies.

The incorporation of CO_2 laser also required careful investigation of the optimal settings to engrave the microchannels with the desired dimensions. Apart from determining the optimal settings of the machine, determining adequate post processing techniques was also fundamental for the proper bonding and overall functionality of the platform. Numerous bonding techniques, amenable to large scale manufacturing, such as low surface energy adhesives, double sided

polymer adhesives, lamination, solvent welding, and thermal fusion bonding where thoroughly investigated.

Each step of the fabrication protocol was carefully calibrated to obtain a successful yield until it became reliable and reproducible. A complete synergy between each step was critical to obtain a final fabrication protocol amenable for manufacturing.

4.1 Channel architecture iterations

The transition process from traditional soft-lithography to digital manufacturing techniques resulted in 4 major modification of the microfluidic channel network architecture (Fig. 7). The first design consisted of an 80-channel network leading to a single outlet. The design was only compatible with soft-lithography fabrication techniques, using silicon wafers, mainly due to the microchannel dimensions. The second design was made following the same fabrication protocol, but it was based on a 40-channel architecture to solve problems related to assembly and variance in resistance across channels.

	CAD Design	Total Channels	Fabrication Method(s)	Material(s)	Fabrication Time
a.	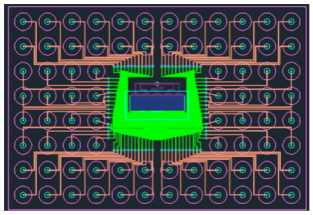				
		Multilayer 80 Channel Network			
		80	Photolithography Soft lithography	Silicon Wafers PDMS Glass	280 minutes
b.	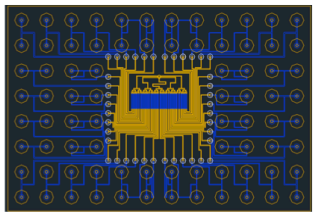				
		Reduced Multilayer Channel Network			
		40	Photolithography Soft lithography	Silicon Wafers PDMS Glass	280 minutes
c.	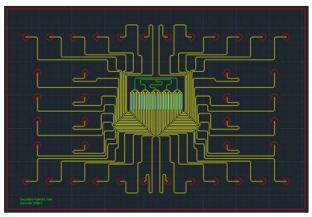				
		Single Layer Channel Network			
		40	Laser CO2 engraving Thermal Fusion Bonding	500µm PMMA 125µm PMMA	28 minutes
d.	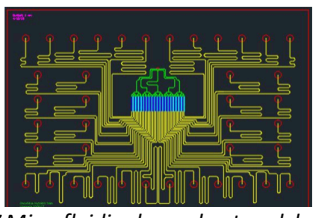				
		Optimized Single Layer Channel Network			
		40	Laser CO2 engraving Thermal Fusion Bonding	300µm PMMA 125µm PMMA	28 minutes

Figure 7 Microfluidic channel network layer iterations a) Multilayer 80 Channel Network fabrication specifications and time. b) Reduced channel network multilayer channel network fabrication specifications and time. c) First single channel network layer fabrication specifications and time. d) Optimized single layer channel network fabrication specifications and time.

Even after the first modification, the second design still took almost 7 hours to complete and it was still not completely reproducible. This led to the complete transition digital manufacturing techniques and, consequently, to a compatible design made with only one material. This resulted in two additional iterations of the channel network design, which led to our current and final design.

4.1.1 First microfluidic architecture

The original platform included a microfluidic channel architecture of 80 different channels connected to a common outlet (Fig. 7a). This design was only compatible with photolithography and soft-lithography fabrication processes. These processes made the fabrication of this part of the platform highly time consuming and low yield; it took almost 5 hours to develop a channel network and only 1 out of 10 came out fully functional. This was a direct consequence of challenging bonding and alignment steps. The channel network consisted of 3 PDMS channel layers and a glass slide, all of which had to be carefully aligned and bonded using plasma. Apart from problems related to its fabrication, the channel network was limited to a 15% variance in resistance across the 80 channels. The main limitation was space; there was not enough space to modify the length nor width of the channels to obtain a lower variability. After careful consideration of all these issues, the most appropriate solution was a complete redesign of the architecture.

4.1.2 Redesign of microfluidic architecture with equivalent resistances

The first redesign aimed to solve the problems related to reproducibility and variance in channel resistance. The channel network was modified to only have 40 delivery channels instead of 80 (Fig. 7b). This modification simplified the alignment and bonding steps leading to a greater reproducibility. Additionally, the reduction in the number of channels, resulted in more space allowing for a greater control of channel resistance. The lengths and widths of each channel was assessed and altered accordingly resulting on ~5% variance in the equivalent resistance between delivery channels. Even after solving these two major problems, the time required to fabricate a single channel network was still about 5 hours. Such timing was not amenable for large scale manufacturing. Nevertheless, the channel dimensions of the new design made it compatible with digital manufacturing techniques such as laser engraving and micromachining.

4.1.3 Single layer channel network

During the transition to digital manufacturing the channel network design was modified to be a single PMMA layer with 40 channels of equal width (Fig. 7c). The channels were engraved on a 500 μm PMMA sheet using CO_2 laser. After engraving, the open channels of the PMMA channel network were sealed with a 125 μm PMMA sheet through thermal fusion bonding. This process reduced the fabrication time from 280 minutes to just 28 minutes. Most importantly, all the problems related with reproducibility, such as alignment and bonding, were solved. Similarly, having the channel network made of only one material made it more compatible with other

bonding strategies, such as solvent bonding. The main limitation of this design was the difference in equivalent resistances between the channels. The width of every channel remained constant, while the length was highly variable. Additionally, the number of curves in each of the channels also contributed to the total resistance in each of the channels. The height of the channels (500 μm) also resulted on a low resistance. Such low resistance was not capable of efficiently preventing forward flow due to gravity. Finally, it also resulted on a low flow velocity in the delivery channels, leading to a greater probability of cross-talk between drugs at the desired flow rate (2 ml/hr.).

4.1.4 Improved equivalent resistance balance optimal for laser engraving

While maintaining the same fabrication protocol, the final redesign aimed to balance the equivalent resistance across the channel network and to increase resistance. To obtain a balanced resistance between every channel, the length of the channel was modified accordingly. Additionally, each channel included the same number of curves, as they also contributed towards the equivalent resistance (Fig. 7d). Finally, to solve the problems related to forward flow and low fluid velocity, the channel network was engraved on a 300 μm PMMA sheet.

4.2 CO_2 laser for device fabrication

The main drawback of utilizing conventional clean room-based fabrication processes, such as photolithography, is that such techniques are not readily translatable for mass manufacturing. However, alternative rapid prototyping techniques have shown promise on facilitating the translation of microfluidic technologies from the laboratory to the commercial arena. Promising technologies include, embossing methods, injection molding, micro milling, and laser engraving/ablation methodologies. Among these techniques, CO_2 laser micromachining is one of the most promising techniques given its rapid turnaround time, low operational costs, mask/cast-less process, agile design processing, and its ability to process a wide variety of polymers [27]. Moreover, microfluidic systems in PMMA are comparatively easily produced by CO2-laser micromachining [28]. Therefore, we decided to shift our focus towards the incorporation of CO_2 laser micromachining as our main fabrication process.

All of the device components were fabricated using the Universal Laser Systems VLS 3.60 and ILS 12.150D platforms. Specifically, the channel network, the lid and the bottom were made with the VLS 3.60 platform, while the 40 well-plate with the ILS 12.150D. The settings of both platforms were thoroughly investigated and optimized to obtain the desired dimensions for each of the device components.

The VLS3.60 platform is a free-standing platform with a materials processing envelope of 24” x 12” x 9”. This platform offers a 10.6μ CO_2 laser source ranging in power from 10 to 60 watts or one 9.3μ CO2 30 watt or 50-watt laser source [29]. An important feature that allowed the engraving of sub-millimeter microchannels was the air assist. The air assist aids on optics protection and prevented reflow of material into the features of the channel network.

The ILS12.75 is also free-standing platform with a materials processing envelope of 48" x 24" x 12”. This is a dual laser platform that supports a power range of 10 to 150 watts (up to 75 watts with one 10.6u CO_2 laser; up to 150 watts with a second 10.6u CO_2 laser). The ILS12.150D also supports a single 9.3u laser at 30, 50 or 75 watts [30]. The high-power capacity using dual laser allowed to cut through a ¾” PMMA block to fabricate the 40 well-plate.

4.2.1 Laser settings optimization for microchannel engravings in PMMA

The power and speed of the VLS 3.60 platform were carefully optimized through a calibration experiment. The drawings shown in figure 8, served to investigate the optimal settings of the laser. The drawing shown in figure 8a, was used to determine the optimal power and speed for the desired channel dimensions. The same drawing was used keeping a constant speed while using different power settings ranging from 0 to 100% (P1, P2, P3…). Similarly, the optimal settings for the desired channel separation were determined using the drawing shown in figure 8b. The separation varied from 75µm to 800µm. The calibration was accomplished by assessing the correlation of power and speed to channel widths and depths (Figs. 9 & 10). With the calibration of the platform we were able to engrave the channel network with the desired features and dimensions. The first engravings were made on both a 500 µm and 300 µm clear PMMA sheet. Similarly, the power and speed of the ILS 12.150D platform were optimized to fabricate the 40 well-plate. However, since the only requirement was to cut through a ¾” clear PMMA block, the power was maintained at 100%, while the speed was adjusted accordingly.

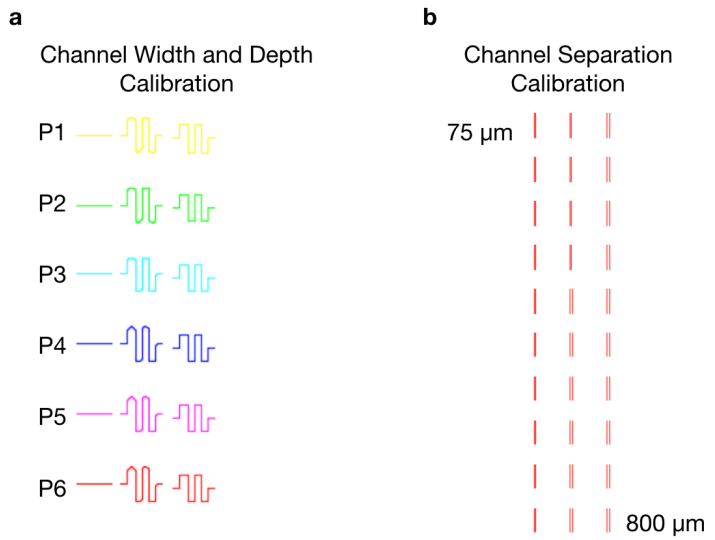

Figure 8 Drawings for ULS VLS 3.60 CO2 laser setting calibrations a) CAD design for channel width and depth calibration. Each color represents a different speed setting. b) CAD drawing for channel separation calibration. Channel separation varied from 75 µm to 800 µm.

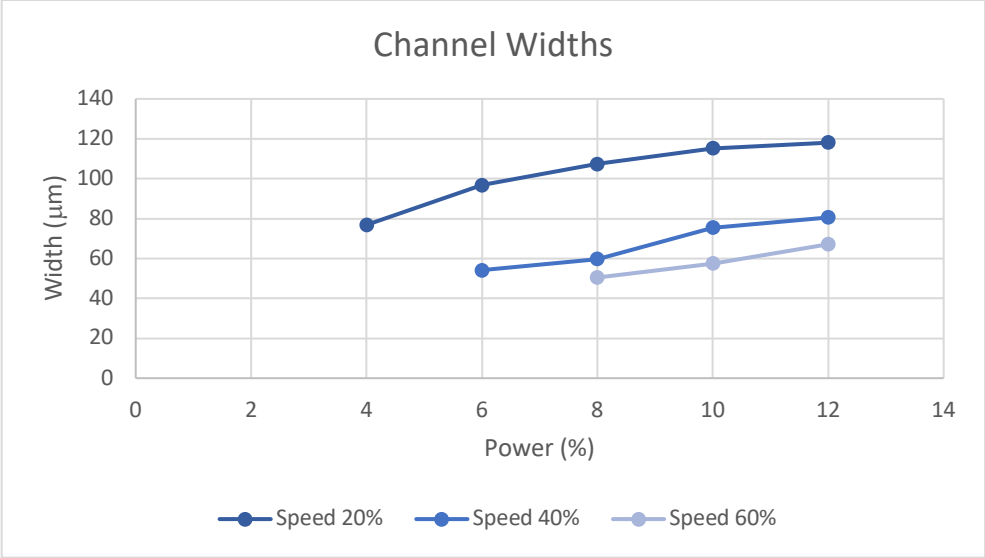

Figure 9 Correlation VLS 3.60 CO2 laser power and speed to channel widths

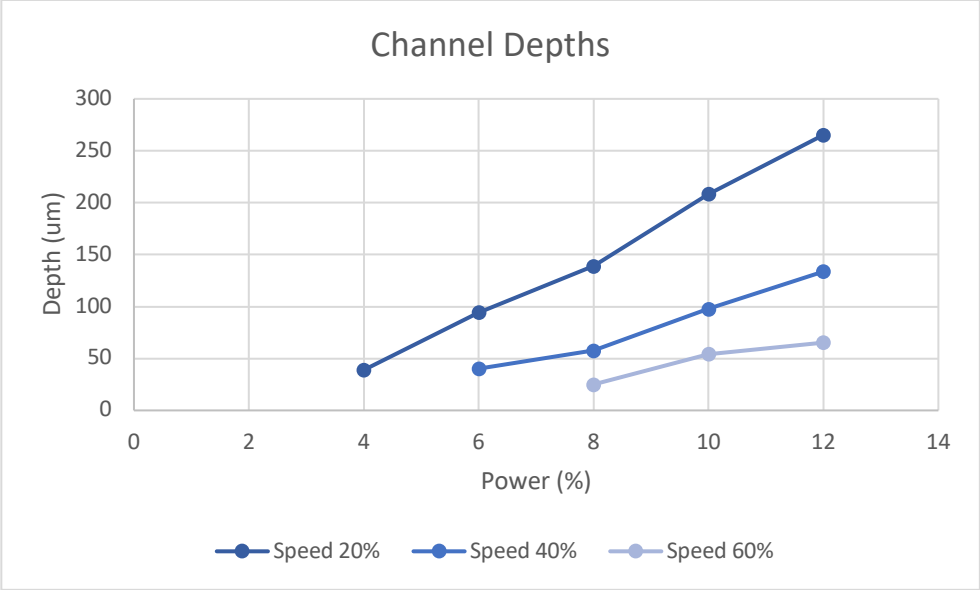

Figure 10 Correlation of VLS 3.60 CO2 laser power and speed to channel depth

4.2.2 500 µm channel layer

The first single layer version of the channel network (Fig.7c) was engraved on a clear 500 µm PMMA sheet. As shown in Figure 7c the design consisted of 5 different colors (red, yellow, green, blue, and cyan), each specifying a different laser setting (Table 4). The yellow setting is used to engrave the 40 delivery channels that connect to the open lanes. Similarly, the green setting engraves the slightly wider outflow channels that connect to the outlet. The blue and cyan settings cut the open channels in the central culture chamber; this setting was performed three times to go through the whole 500 µm. Finally, the red setting performs the through-cuts such as the vias and the outlet. The dimensions of the features were measured with a scanning

electron microscope (Fig. 11). The open drug lanes (Fig.11a) had a trapezoidal geometry with a height of 500 μm, an upper width of 250 μm, and a lower width of 87 μm. The channels had a semi-elliptical geometry with a depth of 81 μm and width of 122 μm.

Table 4 CO2 laser settings for 500 μm channel network

Color	Mode	Power	Speed	PPI	Z-axis
Yellow	Vector	8.0%	40%	1000	0.126”
Green	Vector	8.0%	20%	1000	0.126”
Blue	Vector	10%	30%	1000	0.126”
Cyan	Vector	10%	30%	1000	0.126”
Red	Vector	90%	25%	1000	0.126”

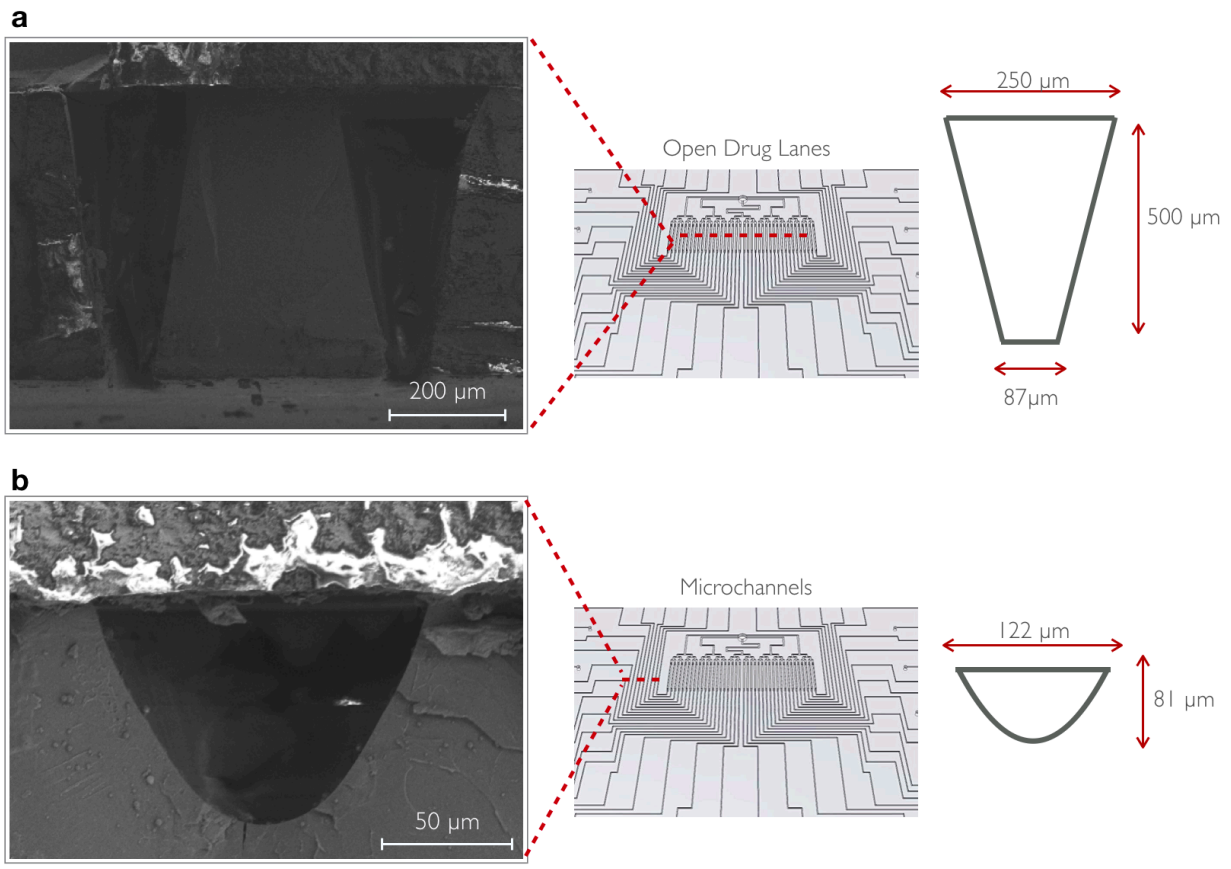

Figure 11 SEM micrographs and measurements of 500 μm PMMA channel network. a) SEM image and dimensions of open drug lanes after laser engraving. b) SEM image and dimensions of microchannels within channel network.

4.2.3 300 μm channel layer

The 300 μm channel network is based on the most recent design (Fig. 7d) and was fabricated using the CO_2 laser settings shown in Table 4. For this version of the channel network, a total of three repeats of the blue and cyan settings had to be performed to successfully engrave the open drug lanes. As for the 500 μm channel network, the dimensions of the features were measured

with a scanning electron microscope (Fig. 12). The open drug lanes (Fig.12a) had a trapezoidal geometry with a height of 300 µm, an upper width of 243 µm, and a lower width of 140 µm. The channels had a semi-elliptical geometry with a depth of 75 µm and width of 130 µm.

Table 5 CO2 laser settings for 300 µm channel network

Color	*Mode*	*Power*	*Speed*	*PPI*	*Z-axis*
Yellow	Vector	8.0%	40%	1000	0.012”
Green	Vector	8.0%	35%	1000	0.012”
Blue	Vector	10%	30%	1000	0.012”
Cyan	Vector	10%	30%	1000	0.012”
Red	Vector	15%	15%	1000	0.012”

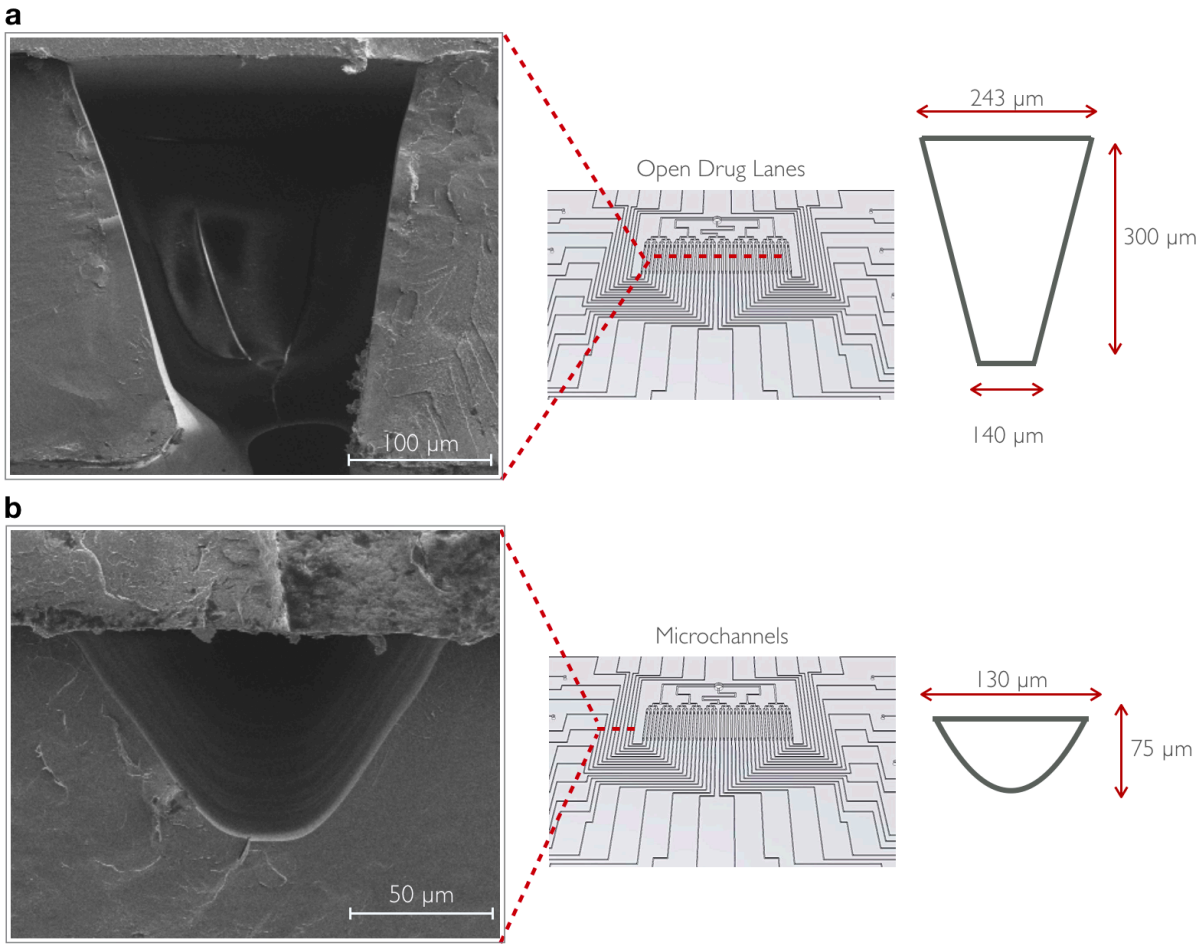

Figure 12 SEM micrographs measurements of 300 µm channel network. a) SEM image and dimensions of open drug lanes after laser engraving. b) SEM image and dimensions of microchannels within channel network.

4.2.4 PMMA 40-well plate design

The 40-well plate shown in Figure 3a is fabricated by cutting a ¾” clear PMMA block with a ULS ILS 12.5D CO_2 laser platform. The fabrication of the 40 well-plate requires a series of steps and a

variety of settings due to the thickness of the PMMA block (Fig. 13). The first step (Fig.13a) is to create a raster cut in the bottom of the plate and the through-hole that will serve as the outlet. The purpose of the raster cut is to prevent over-flow and contact of the methylene chloride with the outlet channels in the channel network during the solvent bonding process of the two parts; without the raster cut, channels were blocked due to methylene chloride overexposure. The second step (Fig. 13b) are the through-cuts of the wells and outline of the plate. This step requires a total of 6 passes; three passes for the wells and outline respectively. The high number of passes is mainly due to the power limit of the laser and to prevent melting of the part. The first pass goes through about 50% of the thickness of the plate. After the first pass, two additional passes at a lower speed are required to go through the whole ¾ "PMMA block. Finally, the purpose of the final step (Fig. 13c) is to create a small well to seal the outlet. It is important to note that before this step, the plate is removed from the laser and clamped between two cold metal plates to prevent deformation resulting from high heat exposure. After the plate cools down it is flipped and replaced in the laser bed. A first pass is required to re-align the plate with the drawing. Once the plate is correctly aligned, the outlet well is made with a raster cut.

CAD Design

a

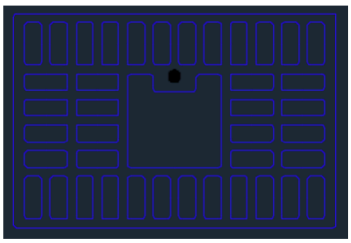

b

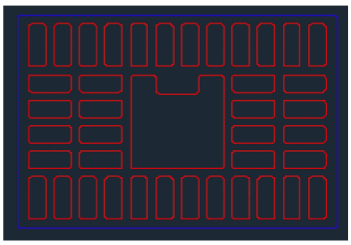

c

ILS 12.5D CO2 Laser Settings

Outlet Trough-Cuts & Raster				
Pass #	Color	Power	Speed	Type
1	Blue	0%	0%	Alignment
2	Black	50%	28%	Raster
3	Red	100%	0.8%	Vector

Well Through-Cuts				
Pass #	Color	Power	Speed	Type
1	Red	100%	4%	Vector
2	Red	100%	2%	Vector
3	Red	100%	0.8%	Vector
4	Blue	100%	4%	Vector
5	Blue	100%	2%	Vector
6	Blue	100%	0.8%	Vector

Outlet Rastering				
Pass #	Color	Power	Speed	Type
1	Blue	0%	0%	Alignment
2	Black	50%	5%	Raster

Figure 13 40 well-plate CAD design, fabrication steps, and ILS12.5D CO2 Laser settings. a) CAD design and laser settings for outlet through-cuts & raster. b) CAD design and laser settings for well through-cuts. c) CAD design and laser settings for alignment and outlet raster.

4.2.5 PMMA Accessories (Lid/Bottom)

The lid and bottom shown in Figure 3a, were also fabricated by cutting clear 1/8" and 1/4" PMMA sheets with the ULS VLS 3.60 CO_2 laser platform. Both of these components are made up of different parts that are bonded using double sided 300 LSE adhesive (Fig. 14); the 300 LSE adhesive is bonded to the PMMA sheet before cutting to facilitate assembly. The lid is made up of a total of three different pieces (Fig. 14a, b, & c). The first piece (Fig. 14a) is the top piece, which shows an outline of the wells and their numbers. The second piece (Fig. 14b), serves as part of an overhang to allow gas exchange and prevent contamination; the triangular corners showed in the CAD drawing serve as a step that sits on top of the 40 well-plate. Finally, the third piece of the lid adds the overhang to complete the structure of the lid, resembling the shape of a conventional 96 well-plate lid (Fig 14c.). The bottom serves as a base to lift the device from the surface. Additionally, the dimensions of the bottom base are based on the dimensions of a 96 well-plate; these dimensions make the platform compatible with microscopes with a conventional plate holder. Similar to the lid, the bottom base consists of two different pieces (Fig. 14c&d). The first part of the bottom base (Fig. 14c) is bonded to the bottom piece (Fig. 14d) to create a base with dimensions that conform with the whole platform.

CAD Design

a

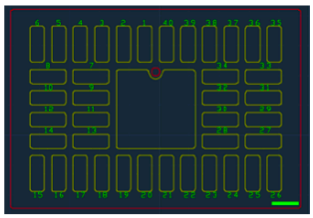

b

c

d

VLS 3.60 CO2 Laser Settings

Lid Top			
Color	Power	Speed	Z-Axis Height
Yellow	80%	20%	0.125"
Green	80%	20%	0.125"
Red	100%	4%	0.125"

Lid Hanger			
Color	Power	Speed	Z-Axis Height
Red	100%	4%	0.125"

Lid Bottom and Bottom Increment			
Color	Power	Speed	Z-Axis Height
Red	100%	1.5%	0.25"

Bottom Base			
Color	Power	Speed	Z-Axis Height
Red	100%	1.5%	0.25"

Figure 14 CAD Design and VLS 3.60 CO2 Laser settings for lid and bottom accessories. a) CAD design and laser settings for lid top engraving and cutting. b) CAD design and laser settings for lid hanger. c) CAD design and laser settings for lid bottom and bottom increment. d) CAD design and laser settings for bottom base.

4.3 Post CO_2 laser processing

Laser machining using CO_2 based systems are known to introduce manufacturing defects and loss of clarity of polymer substrates during fabrication [27]. This occurs as a direct result of the chaotic evaporation and solidification of material as it is removed from the substrate surface by convection forces and the Gaussian power distribution of the laser spot over the areas being processed [28]. These defects can negatively affect functionality and make engraved microfluidics less suitable for optical based biological endpoint analyses due to increased light scattering. Therefore, post-processing methods must be employed to reduce introduced manufacturing defects. Various publications that utilize CO_2 laser as their main fabrication method, recommend that after CO_2 laser engraving and cutting, all the device components should be processed through a DI water rinsing, IPA sonication, and chloroform exposure [27], [28], [31]–[33]. For our platform, these processing steps, served to prevent any channel blockage during thermal fusion bonding of the channel network layer and solvent bonding of the 40 well-plate.

4.3.1 DI water rinsing, IPA sonication, and chloroform treatments

Each device component, especially the channel network, requires thorough rinsing and smoothening after CO_2 engraving. The post engraving protocol was mainly based the work made by Morgan et.al [31]. The protocol established for the channel network layer and the 40 well-plate required vast experimentation; specifically, the determination of rinsing and exposure times. A detailed illustration showing the setup and timing for each component is shown in Figure 15.

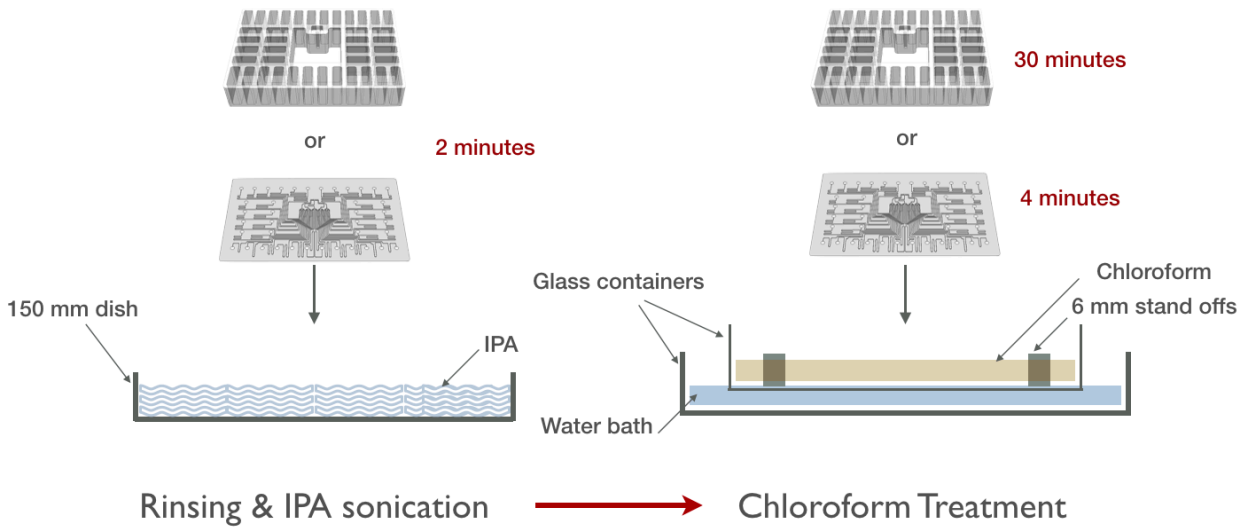

Figure 15 Detailed post processing setup

The importance of post processing for the channel network and the 40 well-plate is illustrated in Figures 16, 17, and 18 respectively. The raw channel network after CO_2 engraving is shown in Figure 16a. This micrograph clearly shows debris accumulation on the microchannels of the network; such accumulation leads to channel blockage and weak bonding due to surface roughness. The first step is to rinse the engraved channel network with DI water. After rinsing, the channel network is submerged in a 150 mm dish filled with IPA and placed in a sonication machine for 2 minutes, rinsed with DI water again, and dried with nitrogen. The resulting channel network is shown in Figure 16b. As shown in the image, even after rinsing with DI water and IPA sonication, the channels still contain debris and the edges of each channel are rough. To get rid of the remaining debris and surface roughness, the channel network is exposed to chloroform for exactly 4 minutes. The chloroform treatment smoothens the surface of the channel network and clears all channels, as shown in Figure 16c.

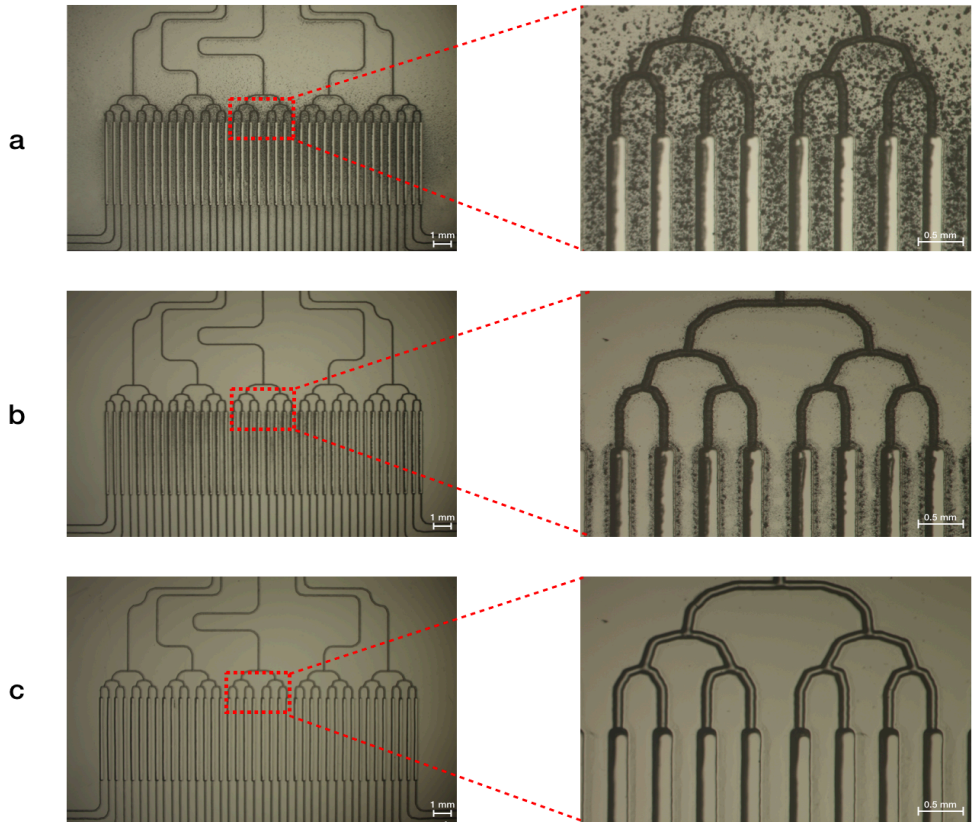

Figure 16 Pre and post processing micrographs of channel network. a) Raw channel network product after laser engraving. b) Channel network after DI water rinsing and IPA sonication. c) Channel network after 4 minutes of chloroform vapor exposure.

To further demonstrate the effect of chloroform vapor exposure, we took SEM images of the channel network before and after exposure (Fig. 16). As shown from both views (top and bottom), the channel roughness is reduced after exposure. Before exposure, it is clear that the channels contain a combination of melted PMMA and reflow after CO2 laser engraving. The vapor

from chloroform exposure successfully removes surface roughness, resulting on a smooth and optically clear channel network.

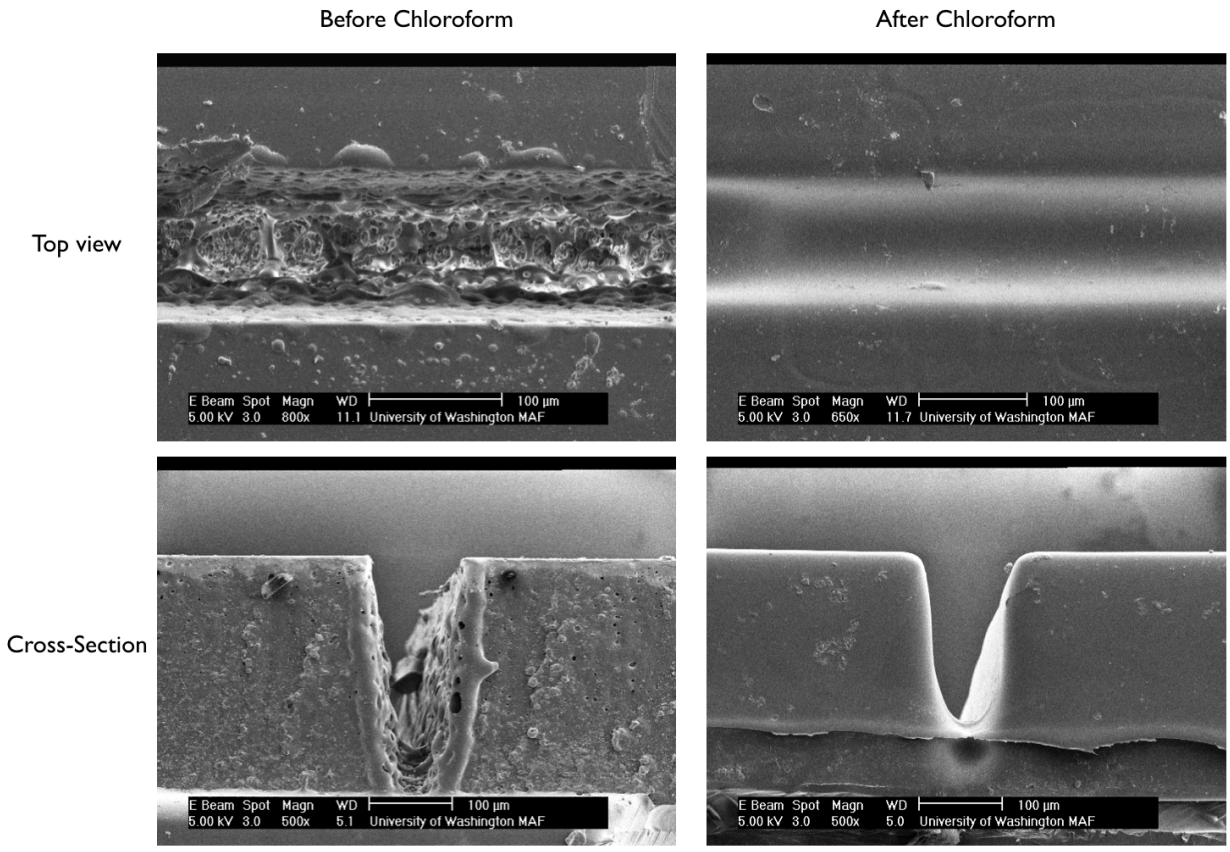

Figure 17 Pre (top) and post processing (bottom) SEM images of channel network

The 40 well-plate undergoes a very similar protocol. The main difference is the chloroform exposure time; the 40 well-plate is exposed for 30 minutes instead of 4 minutes. The main reason is the surface roughness of the PMMA plate after CO_2 cutting and pressing (Fig. 18a). After cutting, the surface of the 40 well-plate has small scratches over the whole surface making it not ideal for solvent bonding. The change in roughness is shown in Figure 18b. After both components are processed with this rapid technique, it is easier to ensure a reliable solvent bonding process. In conjunction with the solvent bonding technique, this process has shown to be an ideal and rapid procedure for the manufacture of PMMA microfluidic devices.

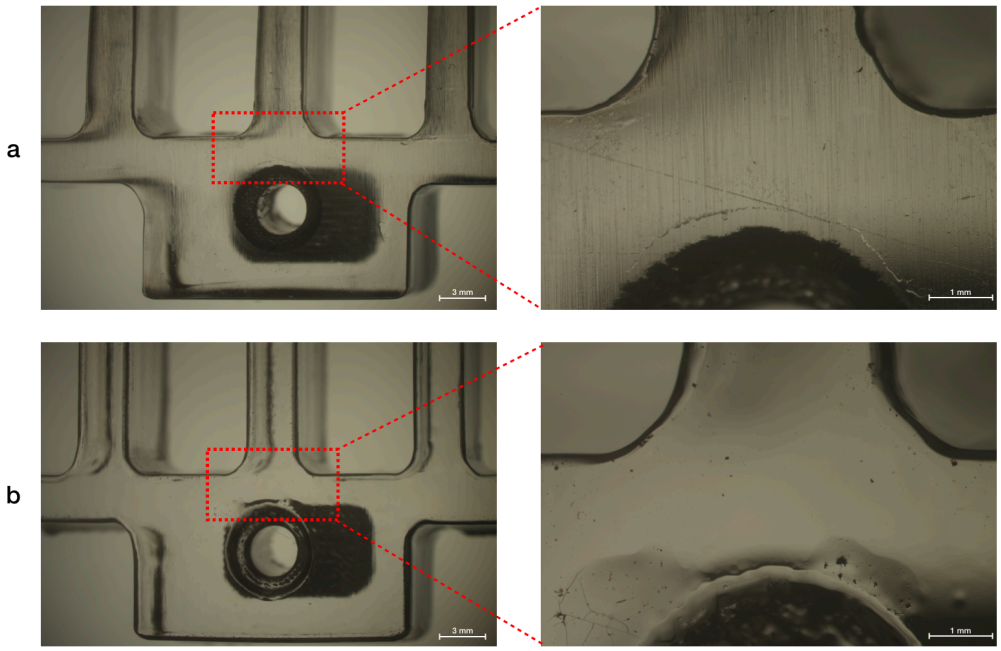

Figure 18 Pre (a) and post (b) processing micrographs of 40 well-plate.

4.4 Bonding Methods

One of the most critical aspects behind the fabrication process of Oncoslice was the bonding methods used for the assembly of its different components. The first version of the platform mainly involved A3648, (3-aminopropyl) triethoxysilane) (APTES) and plasma treatments for PDMS-PDMS, PDMS-glass, and PDMS-polystyrene bonding. After the transition from soft-lithography to digital manufacturing other methods were required for the assembly of the platform. During the transition, a myriad of techniques was thoroughly investigated, such as low surface energy (LSE) adhesives, double-sided polymeric adhesives, PDMS adhesives, high temperature lamination, thermal fusion bonding, and solvent bonding. To assess the effectiveness of each bonding method, we experimented with durability, toughness, hydrophilicity, and, most importantly, biocompatibility. This thorough investigation led to the current bonding methods employed in the assembly of the microfluidic platform.

4.4.1 Conventional APTES and plasma treatments

After the first redesign, the different components of the platform (Fig. 1a) were still being assembled through APTES and plasma treatment bonding methods. The first step was to manually smoothen the bottomless 96 well-plate with a razor. After the plate was manually smoothened, it was cleaned with 70% ETOH, dried with nitrogen, and plasma treated at 670 mm O2/60W for 60 seconds. Once the plasma treatment was completed, the modified well-plate was silane coated with 2% APTES for an hour.

As the plate was being silane coated, the through-hole layer (Fig. 1a) was prepared by manually punching 3 mm holes, followed by an IPA rinse and nitrogen drying. Then, the through-hole layer was plasma treated at 670 mm O2/60W for 60 seconds in preparation for bonding with the plate. As the through-hole layer was plasma treated, the silane coated 96 well-plate was rinsed one last time with distilled water and dried with nitrogen. Once the plasma treatment of the through-hole layer was complete the two components where irreversibly bonded together. Finally, the two bonded components were placed on a hot plate at 80-85C for 5 min.

Following a similar protocol, the PDMS microfluidic chip layer was bonded to a glass slide using plasma. Both of the components were thoroughly rinsed with IPA, nitrogen dried and plasma treated at 670 mm O2/60W for 60 seconds. After plasma treatment the microfluidic chip was bonded to the glass slide. Once this bonding step was completed, the connector layer followed the same protocol and after plasma treatment it was carefully aligned and bonded to the microfluidic chip/glass slide component. The final step was to assemble the microfluidic component of the device, made out of two PDMS connecting layers and a PDMS microfluidic chip bonded to a glass slide, to the 96 well-plate with the through-hole layer. Both, the microfluidic component and the well-plate, were plasma treated at the same conditions, aligned, and carefully bonded together. This process required vast amount of training and considerable expertise. Each step had to be flawlessly completed by ensuring the bond was homogenous, leak proof, and most importantly perfectly aligned.

Evidently, this technique was not ideal for large scale manufacturing as it required a highly trained lab technician, vast amount of labor, and it was not reproducible. The first problem with this bonding strategy usually originated in the first bonding step; the bonding of a rigid polystyrene well-plate to a PDMS through-hole layer. The bottom of the well-plate was usually rough and not smooth enough for a complete and leak-proof bond; manually smoothening the plate with a razor was not sufficient to ensure a homogenous surface. The second problem, as mentioned before, were the alignment challenges. This bonding method had 3 critical alignments that had to be made perfectly to ensure a fully functional device. Finally, this whole process took almost 7 hours to complete. Evidently this was one of the major challenges that had to be solved for the prosperity of the platform.

4.4.2 Indirect adhesive bonding

As the problems associated with conventional APTES and plasma bonding techniques kept slowing the progress of the platform, we decided to begin incorporating several types of adhesives to the different bonding steps of the device. The incorporation of adhesives was made iteratively by assessing each of the problems.

After investigating which adhesives would be ideal to potentially solve each of the problems we were having, we decided to include double sided adhesives to the first bonding step of the assembly process; the bonding of the 96 well-plate to the PDMS through-hole layer. As we

understood how different types of adhesives were used for multi-layered microfluidic devices, we began experimenting with several techniques to improve our fabrication protocol.

The transition to digital manufacturing with CO_2 laser cutting, opened a whole new avenue for us to investigate how low surface energy adhesives were used in the microfluidic and medical device industries. The process mostly involved lining the PMMA substrates with the double-sided adhesive before CO_2 laser cutting/ engraving. The goal of this process was to facilitate alignment and reduce fabrication time by getting rid of plasma bonding completely.

4.4.2.1 Double sided silicone/acrylic tape for polystyrene-PDMS bonding

To eliminate the first problem, related to the bonding of the polystyrene well-plate to the PDMS through-hole layer, we decided to incorporate 3M Double sided silicone/acrylic tape 9699 (Fig.19). The adhesive features a sensitive adhesive coated on one side of a polyester film carrier and a high performance acrylic pressure sensitive adhesive coated on the other side of the carrier [34]. The silicone adhesive provides good bond to silicone rubber and strong holding power to various silicone surfaces, such as the PDMS through-hole layer. The acrylic adhesive offers good shear resistance and adhesion to a variety of surfaces, such as polystyrene.

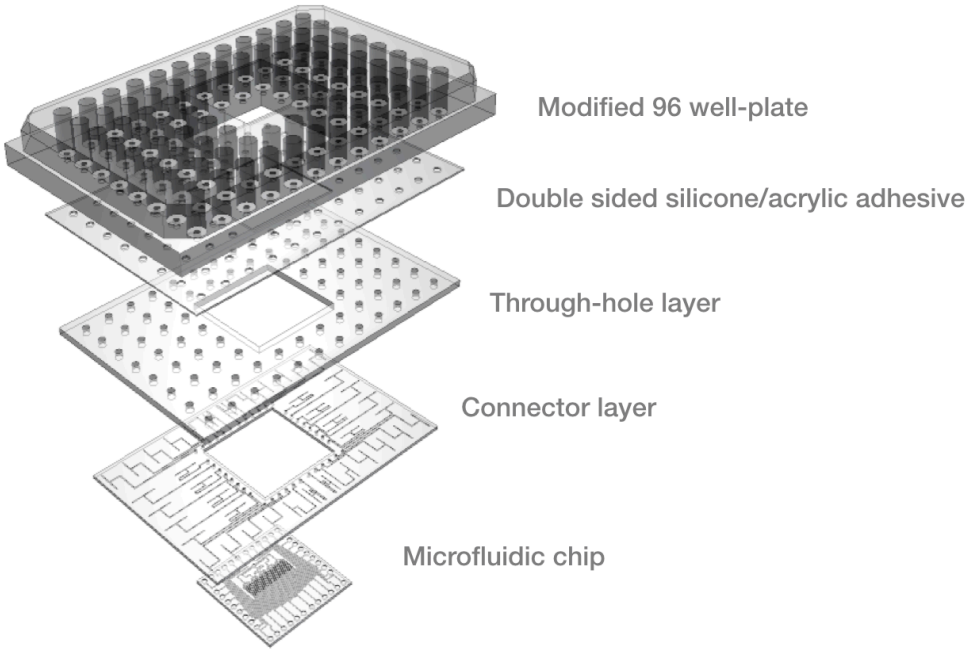

Figure 19 First incorporation of adhesives to bonding protocol

The addition of double sided adhesive to this bonding step of the protocol temporarily solved the problems related to the bonding of the 96 well-plate to the PDMS through-hole layer. It also reduced the fabrication time and got rid of one alignment step. The bonding process was simple, reliable, and efficient. In light of the success we were having with this bonding strategy we began

investigating the possibility of including adhesives for additional bonding steps of the platform. The idea of using adhesives to assemble the whole platform was one of the main drivers to shift towards a device made only of one material. Having read how the adhesives were used in the industry we began exploring the production of the device using PMMA as the main material and CO_2 laser as the fabrication method. We first began exploring the possibility of creating a single channel network made out of PMMA by combining both the connector layer and microfluidic chip into one CAD design and engraving it with CO_2 laser.

After creating the first PMMA CO_2 engraved channel network, we included double sided adhesives to bond it to the 96 well-plate components, which was still polystyrene (Fig. 20). The double-sided adhesive served to bond the channel network to the PDMS through-hole layer. The properties of the adhesive simplified one of the most complex bonding processes of the platform; the alignment and assembly of the channel network to the PDMS through-hole layer.

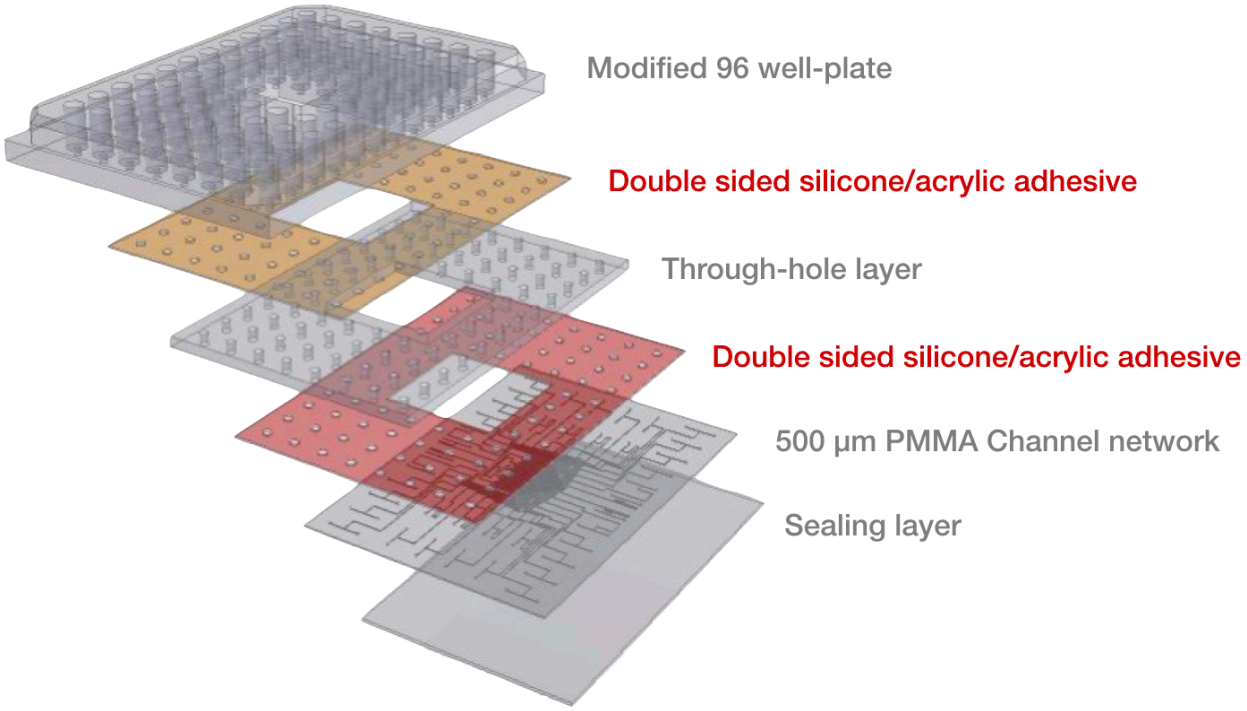

Figure 20 Incorporation of double sided adhesives to additional bonding steps

After having succeeded with this bonding strategy on several occasions, we began testing the performance of built devices through biological experiments. We were able to perform several biological experiments using this bonding strategy, however, the platform did not remain leak proof for more than 3 experiments. This bonding strategy is still widely used and ideal for disposable devices, which are not over-exposed to humid environments. Since this issue directly hindered the durability and reliability of the platform, we continued to explore other types adhesives.

4.4.2.2 PDMS Adhesive

After experimenting with the 3M double sided silicone/acrylic adhesive, we explored polyolefin double coated thin tape bearing a pressure sensitive poly(dimethyl)siloxane (PDMS) adhesive. This adhesive was recommended by Josh Buser at Paul Yager's lab. The adhesive was highly recommended for multi-layer bonding of microfluidic platforms made up of PDMS and other thermoplastics. We replaced the double-sided adhesive with the PDMS adhesive to bond the modified 96 well-plate to the through hole layer (Fig. 19). The bond was very strong and leak proof at room temperature. However, after the platform began leaking after being placed inside the incubator for 24 hours.

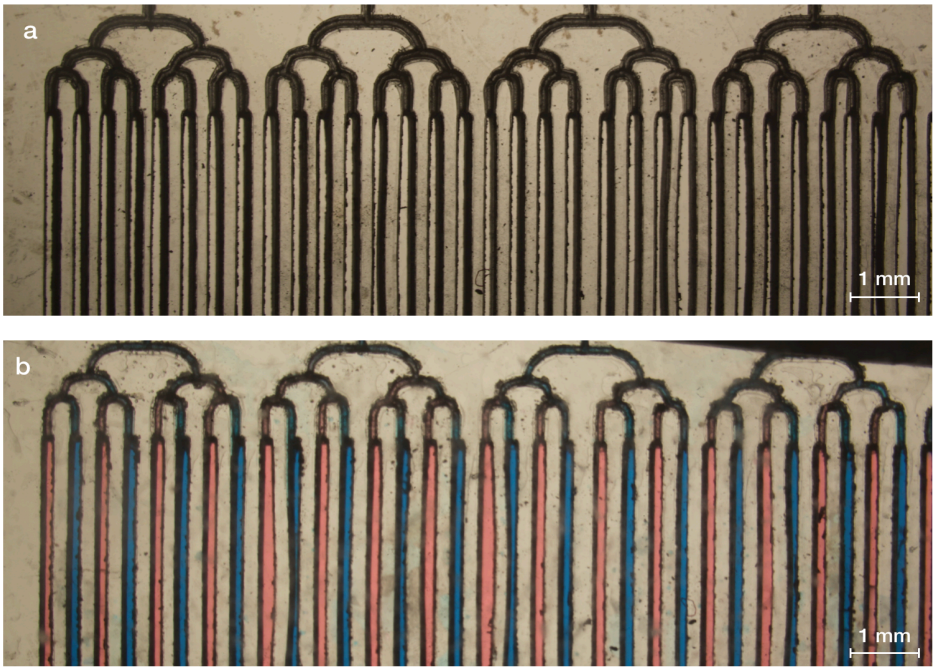

Figure 21 Channel network sealed with PDMS adhesive before (a) and after (b) chloroform exposure

Similarly, the PDMS adhesive was used as the sealing layer for the 500 μm PMMA channel network (Fig. 21). To facilitate the bonding of these two components, one side of the PDMS tape is bonded to the 500 μm PMMA sheet. With the two components bonded, the channel network was engraved using CO_2 laser. The bond between the PMMA channel network and the PDMS adhesive was completely leak proof. The micrograph in Figure 21a shows a sealed channel network with the PDMS adhesive, without chloroform treatment. Clearly, the channels were not completely clean and complicated the functionality of the platform. To prevent this problem, we tried exposing the sealed channel network to chloroform for 4 minutes. After chloroform treatment the channel network was functional, as shown in Figure 21b. However, the channels still contained small debris, which led to their complete occlusion. After careful inspection we were able to observe that the debris inside the channels was PDMS adhesive. Since this was not

observed on the channel network before chloroform exposure, we were able to conclude that chloroform was degrading the properties of the PDMS adhesive. Since we were not able to clean the channel network with chloroform due to this issue we were not able to continue with this adhesive.

4.4.2.3 300 LSE

After assessing the limitations behind of polystyrene-PDMS bonding and the problems with double sided silicone/acrylic and PDMS adhesives, we decided to completely transition to fabrication using PMMA thermoplastics. The first modification of the platform was the incorporation of a PMMA 40 well-plate. The first design included a total of 3 ¼" inch PMMA plates (Fig. 22). The main reason behind having three plates was the power limitation of the VLS 3.60 laser system; with its maximum focus and power ¼" is as much as it safely can cut through. To facilitate the bonding of all the components we used 3M 300 LSE double sided adhesive. The adhesive tape features an internal carrier, such as polyester film, tissue or paper. The internal carrier is coated on both sides with specialty formulated 300 LSE adhesive and then matched to a removable liner. Moreover, the adhesive provides high bond strength to most surfaces, including many low surface energy plastics such as polypropylene and PMMA [35].

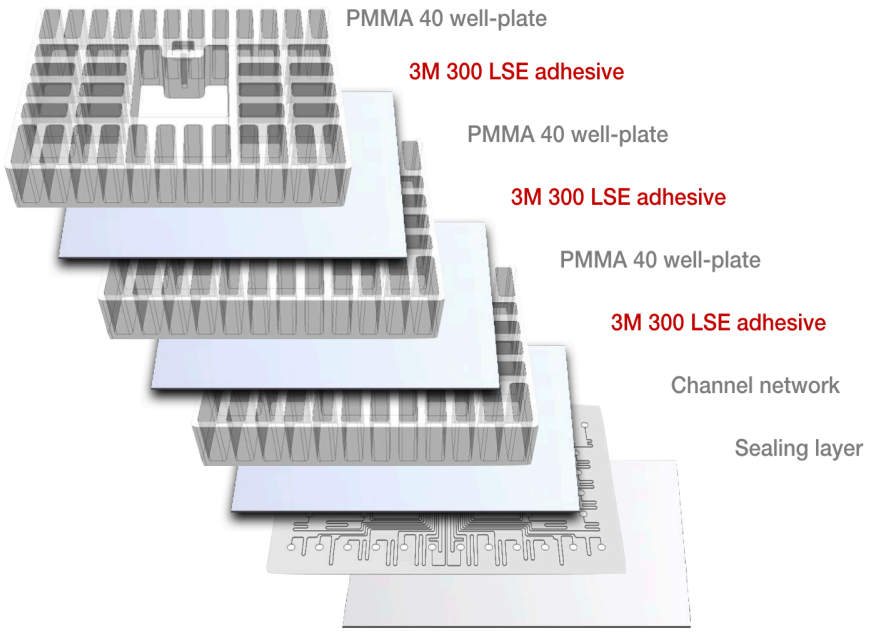

Figure 22 3M 300 LSE bonding strategy overview

To facilitate the alignment, the 300 LSE adhesive is transferred to the top surface of the ¼" PMMA substrate prior to CO_2 laser cutting. As shown in Figure 20, the adhesive was placed on both sides of the PMMA sheet for the middle and bottom plate. After laser cutting, the plates were carefully

aligned, bonded together, and pressed at 200 psi for 2 minutes. Finally, once the ¾" PMMA is completely bonded, it was aligned and assembled to the previously sealed channel network.

Apart from using the 300 LSE adhesive for the bonding of the three ¼ "PMMA plates, we also tried using the adhesive as the sealing layer of the channel network. Following the similar process used for the PDMS adhesive, the 300 LSE was lined on a 500 μm PMMA sheet. With the 300 LSE as the liner, the channel network was laser engraved. We were able to obtain a leak-proof bond, but we encountered the similar issues as seen with the PDMS adhesive. The adhesive properties of the tape were degraded after chloroform exposure and the resulting channel network was also very hydrophobic (even after plasma treatment).

4.4.3 Lamination techniques

Apart from low surface energy adhesives, laminators have been employed to circumvent the need for complex instrumentation and chemicals for the assembly multilayered microfluidic devices. Landers et. al presented a technique for fabricating microfluidic devices with complex multilayer architectures using a laser printer, a CO_2 laser cutter, an office laminator, which they refer to as the laser print, cut, and laminate (PCL) methodology [36]. Apart from the laser printing, their protocol resembled the fabrication process of our platform. To simplify the channel network fabrication process, we decided to experiment and, possibly, integrate their lamination strategy to our protocol.

Landers et.al utilized the office laminator Akiles UltraLam 250B to bond 2–7 layers of transparencies. With the incorporation of this machine to their protocol they were able to demonstrate rapid prototyping of complex, multilayer microfluidic architectures in <1 hour with sparse resources and common laboratory equipment. In light of their success, we began investigating the bonding of the channel network using the Akiles ProLam Ultra X6 laminator (Fig. 23). Following the process shown in Figure 23, we experimented the bonding of the PMMA channel network layer to PMMA and PET by altering the temperature (0˚C - 140˚C), lamination speed (9 speed settings, max speed ~ 1500 mm/s), and number of lamination passes. After lamination, we investigated the durability of the bond by immersing the substrates in PBS and placing them in the incubator (37°C, 95% relative humidity and, 5% CO_2 level) for 12+ hours.

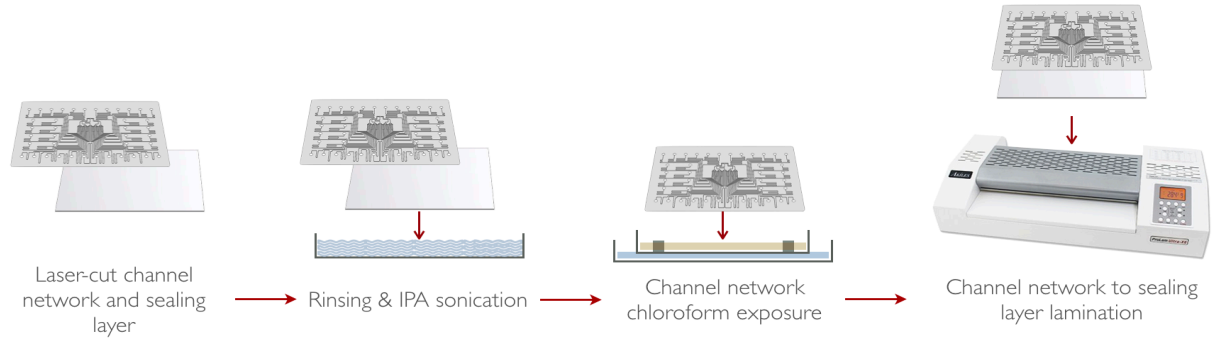

Figure 23 Channel network lamination protocol

4.4.3.1 PMMA-PET

The first lamination attempts involved laminating the engraved and chloroformed 500 μm PMMA channel network with a PET sealing layer. The main advantages of the PET laminate were that it is biocompatible and has hydrophilic properties. The testing method involved alternating the speed, temperature, channel orientation, and number of times the substrates were laminated. Knowing that the glass transition temperature of PMMA is between 85 ˚C - 110˚C, we were to focus on alternating speed, channel orientation, and number of laminations. After focusing on the speed of lamination setting, we were able to conclude that the speeds below 4, were to slow and melted the whole channel network. Subsequently, we focused on the orientation of the channel network as it was placed in the lamination machine. We were also able to conclude that if the channels were perpendicular to the orientation of the machine, the channels would melt completely. In the end, we were able to narrow down the variables to two temperature settings (110˚C & 130˚C) and 4 speed settings (4,5,6,7). After sampling each combination of the pooled settings, we inspected each the resulting substrates. An example of this process and one substrate is shown in Figure 24.

This micrograph illustrates the three main problems we were encountering: warping, peeling, and melting of the channels. The substrates that had none of these problems were tested by submerging them in PBS and placing them in a cell culture incubator for 24h. Unfortunately, we were not able to get rid of the warping completely and the bond was not durable; after incubation all of the substrates peeled easily. Our main conclusion was that these issues were due to the different material properties of the materials used.

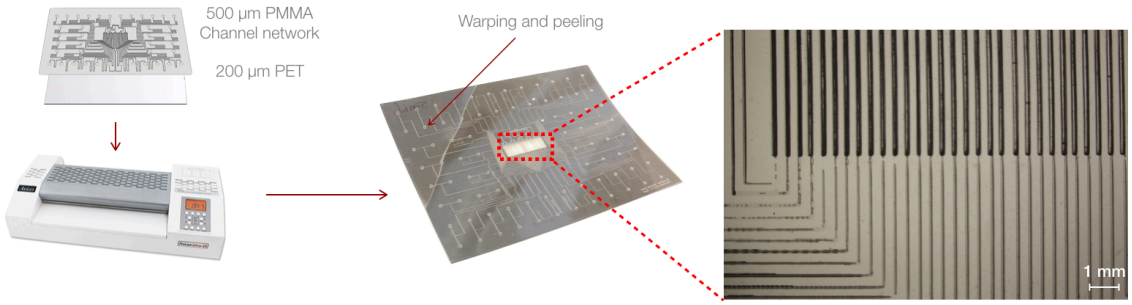

Figure 24 PMMA-PET Lamination

4.4.3.2 PMMA-PMMA

After carefully assessing the problems associated with the lamination of PMMA-PET, we decided to test PMMA-PMMA lamination. Similarly, the 500 μm PMMA channel network was sealed with a 125 μm PMMA instead of the PET laminate. After following the same variable selection process explained on the previous section, we were able to reduce the variables to two temperature settings (110˚C & 130˚C) and 4 speed settings (1, 2, 3, & 4). After sampling each combination of

the pooled settings, we inspected the resulting substrates (Fig. 25). As shown in Figure 25, we were not observing warping and/or peeling after lamination. However, depending on the settings, we began to observe formation of air pockets, melting of channels, and what appeared to be crystallization. We believe that PMMA crystallized after being pressed near its glass transition temperature. Following the same testing protocol, we selected the substrates that had none of these problems and tested them by submerging them in PBS and placing them in a cell culture incubator for 24h. Compared to the PMMA-PET laminations, only the substrates with settings 130˚C and speed 2 were durable in incubation and did not warp. Having determined the appropriate lamination settings several devices were built using this bonding method for the channel network. Unfortunately, we were able to observe how the crystallization of PMMA began to negatively affect the functionality of the platform by blocking the delivery channels.

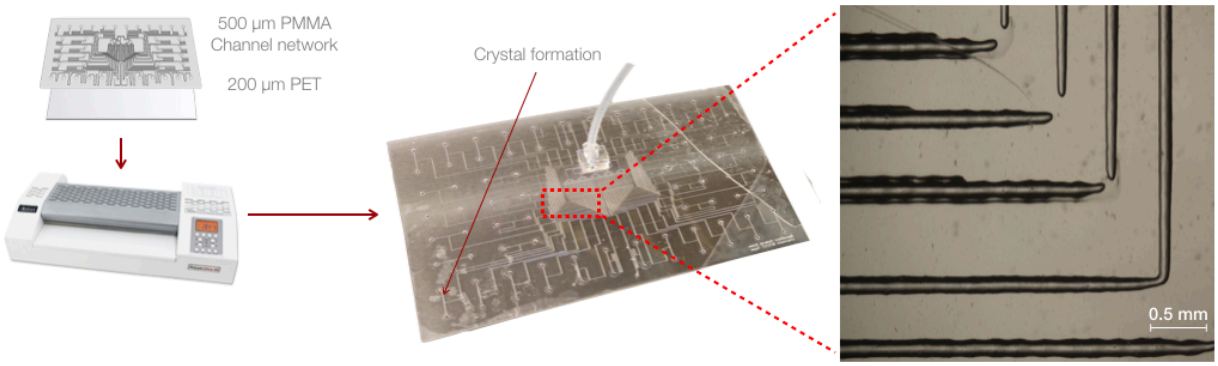

Figure 25 PMMA-PMMA Lamination

4.4.4 Solvent bonding

Thermal fusion bonding, and solvent bonding remain the most prevalent bonding methods applied to thermoplastic microfluidics [32]. These techniques are attractive because they are able to seal the joint between two plastic substrates, and, in addition to bonding, minimize surface damage and maintain a very aesthetic design [37]. In comparison to other mechanical fasteners, solvent bonding forms a joint that is uniform, resulting on an even and homogenous stress distribution. This bonding process is also relatively simple and is amenable for high production throughput. The method involves solvating the bonding surface by applying the solvent as a liquid or vapor phase. The solvent causes the polymer chains to become mobile, allowing for diffusion between the two substrates, leading to an extensive polymer chain entanglement across the interface [37] .

The only drawback is that the mechanical properties of solvent treated thermoplastics could be lower than the virgin thermoplastic; a solvent treated PMMA substrate could likely have a lower tensile and shear strength compared to its virgin PMMA [37].Usually, solvent uptake should be

controlled and minimized to reduce channel distortion of the microfluidic device during the bonding process. This can be controlled by balancing the solvent exposure time and required bonding strength.

To further optimize the fabrication process of our platform we incorporated these two different solvent bonding techniques to the fabrication protocol of the platform. The first technique commonly known as thermal fusion bonding, involves exposing a polymer substrate (PMMA) to an organic solvent, such as chloroform, followed by thermally assisted pressing. This technique was employed for the sealing of the channel network. The second technique is a very similar process involving the exposure of a polymer to an organic solute directly without thermal assist. For our protocol we investigated the bonding properties of the PMMA 40 well-plate after exposure to methylene chloride. In order to control and minimize channel distortion and melting, we had to carefully investigate the appropriate solvent exposure time and pressing parameters (temperature, pressure, and time).

4.4.4.1 Thermal fusion bonding

During thermal fusion bonding substrates are heated to a temperature near or above the glass transition temperature of one or both of the substrate materials, while applying a pressure to increase mating contact forces [32]. The combined temperature and pressure are able to generate sufficient flow of polymer at the interface to achieve intimate contact, with interdiffusion of polymer chains between the surfaces leading to a strong bond. Under ideal conditions, the resulting bond strength can reach the cohesive strength of the bulk material [32].

By following a thermal fusion bonding protocol by Morgan et.al, we established a baseline for both the chloroform exposure time and the heat press settings (temperature, pressure, and pressing time) [32]. In this set of experiments, we investigated using a 500 μm PMMA and a 125 μm PMMA sheet to seal the 500 μm PMMA channel network. The chloroform exposure of the channel network had been already determined to be 4 minutes, as it was the required time to clear and smoothen all the channels. In order to find the appropriate settings for this bonding technique, each variable was controlled independently.

Since the protocol established by Morgan et. al, did not specify the press model nor the pressing surface area, the first step was to determine the ideal pressing force for the surface area of the Carver Inc. 4126 Heat Press (Table 6) [31]. The other thermal fusion bonding conditions were specified in the protocol, therefore, we decided to test the bonding using a press force ranging from 120 – 200 psi. After inspecting each setting under the microscope, we were able to determine that 130-160 psi showed the best bond. Nevertheless, we observed repeated melting of channels along the network interface, therefore, we still needed to optimize other conditions.

Table 6 Pressing force optimization

500 μM PMMA SEALING LAYER - PRESS FORCE

CONSTANTS: PRESS TEMP.: **60˚C**, PRESS TIME: **20 MIN.**, CHLOROFORM EXPOSURE: **4 MIN.**

FORCE (PSI)	**Resulting Bond**
120	Partial Bond and visible air pockets
140	Partial bond
160	Complete bonding, slight melting of channels
180	Channel melting and distortion (20/40)
200	Channel melting (20/40)

To further optimize the bonding conditions, we focused on the pressing time and kept the rest of the conditions constant. Based on the idea that pressing for 20 minutes was probably causing the melting of the channels, we decided to investigate lower pressing times (Table 7). After testing each condition, we were able to determine that 20 minutes was not necessary to obtain a complete bond and that 10 minutes showed the best results. However, we were still observing melting of the channel network at unusual places along the interface. Therefore, the remaining conditions had to be altered.

Table 7 Table 6 Pressing time optimization

500 μM PMMA SEALING LAYER - PRESSING TIME

CONSTANTS: PRESS TEMP.: **60˚C,** PRESS FORCE: **160 PSI,** CHLOROFORM EXPOSURE: **4 MIN.**

PRESSING TIME (MINUTES)	Resulting Bond
5	Partial Bond and visible air pockets
10	Complete bonding
15	Complete bonding (15/40 melt)
20	Complete bonding (20/40 melt)

Since 60˚C is the temperature employed by Morgan et.al and Tay et.al, the chloroform exposure time of the 500 μm PMMA sealing layer was the logical condition to investigate. As shown in Table 8, we tested for chloroform exposure time ranging from 0 to 4 minutes, while keeping all the other optimized conditions constant. After careful inspection of the channel network of each sample, we observed that chloroform exposures between 2 and 3 minutes were ideal for our protocol. Based on these results we decided to maintain the chloroform exposure for 2 minutes.

Table 8 500μm PMMA sealing layer chloroform exposure time optimization

500 μM PMMA SEALING LAYER - CHLOROFORM EXPOSURE TIME

CONSTANTS: PRESS TEMP.: **60˚C,** PRESS FORCE: **160 PSI,** PRESS TIME: **10 MIN.**

CHLOROFORM EXPOSURE TIME (MINUTES)	**Resulting Bond**
0	Weak and partial bond, numerous air pockets
1	Partial bond and visible air pockets
2	Complete bond
3	Complete bond

4	Complete bond (10/40 melt)

After determining all the conditions for thermal fusion bonding with chloroform, we successfully fabricated perfectly sealed 1 mm PMMA channel networks. This technique resulted on an optically clear and aesthetic channel interface. Additionally, the bond remained leak proof after 24 hours of incubation (37°C, 95% relative humidity and, 5% CO_2 level). Unfortunately, due to the thickness of the sealing layer and its rigidity, we began encountering problems with its bonding to the 40 well-plate.

To solve this problem, we decided to use a 300μm channel network and a 125 μm PMMA sealing layer instead; decreasing the thickness of the channel network would make it more compliant and amenable for bonding to the 40 well-plate. As done previously, we began by testing a range of chloroform exposure times to ensure the conditions were still optimal for thermal fusion bonding.

The results demonstrated that the optimal exposure time was still between 2 to 3 minutes. Consequently, we maintained a chloroform exposure of 2 minutes. After this iterative process, we were able to determine the optimal thermal fusion bonding conditions for the complete fabrication of the PMMA channel network (Table 10). These conditions are currently employed in the fabrication protocol of the platform.

Table 9 125μm PMMA sealing layer chloroform exposure time optimization

125 μM PMMA SEALING LAYER - CHLOROFORM EXPOSURE TIME CONSTANTS: PRESS TEMP.: **65˚C,** PRESS FORCE: **160 PSI,** PRESS TIME: **10 MIN.**	
CHLOROFORM EXPOSURE TIME (MINUTES)	**Resulting Bond**
0	Weak and partial bond, numerous air pockets
1	Partial bond and visible air pockets
2	Complete bond
3	Complete bond (5/40 melt)
4	Complete bond (10/40 melt)

Table 10 Optimal conditions for thermal fusion bonding

CONDITION	OPTIMAL SET POINT
PRESSING TEMPERATURE	65˚C
PRESSING TIME	10 minutes
PRESSING FORCE	160 psi
CHANNEL NETWORK CHLOROFORM EXPOSURE	4 minutes
SEALING LAYER CHLOROFORM EXPOSURE	2 minutes

4.4.4.2 PMMA Solvent bonding with methylene chloride

In light of the success of thermal fusion solvent bonding of the PMMA channel network, we decided to investigate a similar solvent bonding process to assemble the PMMA 40 well-plate to

the channel network. A publication by DeVoe et.al made emphasis on the ideal solvents for solvent bonding of PMMA microfluidic substrates. Devoe et.al, explain that for interactions between organic solvents and polymers, solubility can be adequately described by the Hildebrandt parameter, defined as δ $(J/cm^3)^{1/2}$. The Hildebrandt parameter provides a measure of the cohesive molecular forces for both solvent and solute. If the cohesive forces for each material are similar, their molecules can readily co-exist, and dissolution of the solute will occur. PMMA has a solubility parameter of 20.1 $(J/cm^3)^{1/2}$, while methylene chloride has a has a solubility parameter of 19.8 $(J/cm^3)^{1/2}$, making it an ideal solvent for strong cohesive molecular forces [32].

With this information we decided to experiment with 99% methylene chloride as the solvent for PMMA bonding. It is important to note that, first, the surface of the PMMA 40 well-plate was exposed to chloroform vapor for 30 minutes. This ensures a homogenous and uniform stress distribution along the interface of the two substrates during solvent bonding. After the chloroform treatment, the surface of the PMMA 40 well-plate was submerged in a methylene chloride bath for ~15 seconds; enough time to achieve solvation of the surface. The plate was immediately removed and hand bonded to the PMMA channel network. Finally, once the two substrates were in complete contact, they were placed on a press for 5 minutes at 180 psi. The assembled platform had a high bond strength and remained leak-proof after several days of incubation.

The incorporation of thermal fusion bonding and solvent bonding has made the fabrication protocol of the device suitable for high-throughput production; both processes are fast, highly reproducible, and low-cost. Most importantly the compatibility of these bonding techniques with CO_2 laser cutting/engraving augments the potential of the device to scale from laboratory prototyping to full scale mass production.

4.5 Outlet Design

The outlet is one of the most critical components since it dictates the overall functionality of the platform. The first version of the platform included an outlet made out of PDMS, which was manually bonded to the channel network (Fig. 26a).

Before bonding, the PDMS piece had a manually punched through hole to fit a metal pin. The PDMS piece was plasma bonded to the surface of the culture chamber by carefully aligning it to the common outlet of the channel network. Finally, the metal pin was carefully inserted in the punched hole.

Apart from being a complicated and meticulous process, the outlet would easily tear if the metal pin was moved during experimentation. As shown in Figure 26b, the metal pin caused shear stress on the PDMS piece every time it was moved around. Additionally, there was a big risk of removing the pin or the outlet as a whole if the user pulled the tubing attached to the metal pin

with excessive force. If the metal pin was removed by accident, it could not be replaced, since any small piece of PDMS would clog the main outlet source of the channel network.

Overall, this outlet design was very fragile, and, consequently, it required significant improvement. After several experiments were halted by outlet malfunction, we decided to begin investigating potential outlet alternatives to solve the problem. As the platform transitioned from soft-lithography based platform to thermoplastics and digital manufacturing, different strategies were followed to solve the problems related to outlet design and functionality.

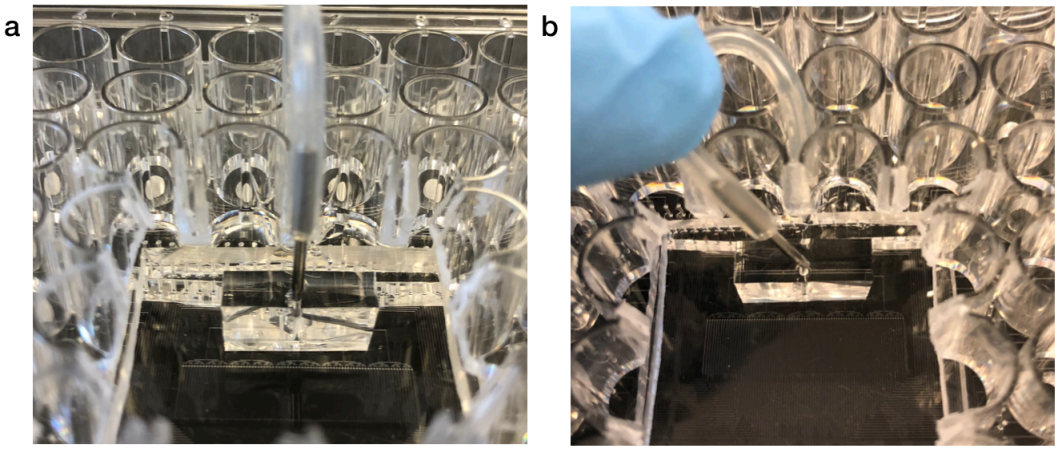

Figure 26 First outlet design a) PDMS piece with an inserted pin b) Demonstration of stress induced by metal pin

4.5.1 Conventional PDMS molded outlets

To solve the problems resulting from the metal pin, we designed, and laser cut a mold out of PMMA to create outlet connectors with embedded tubing (Fig. 27a). The outlets were fabricated by assembling the PMMA mold and filling it with PDMS (Fig. 27b). After curing, the mold was disassembled, and the outlets were ready to bond (Fig. 27c). The main advantage of this design was that it made the outlet more resistant to shear stress.

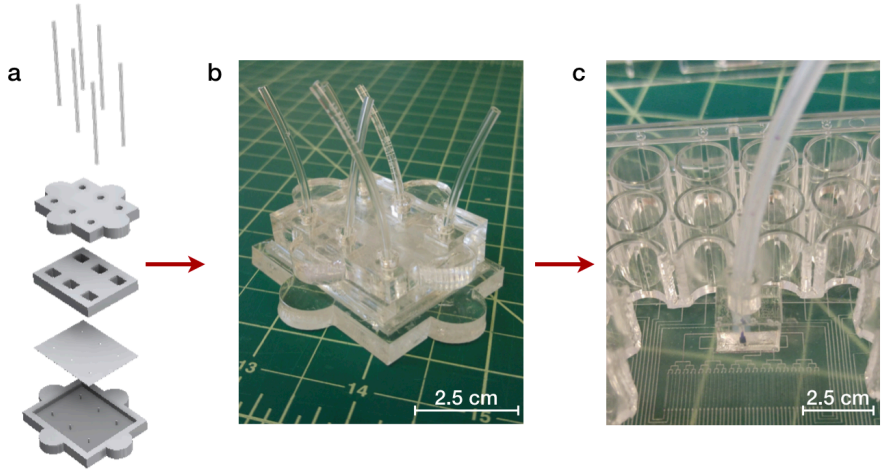

Figure 27 PDMS molded outlets

At this stage of the platform design, the channel network was being fabricated using PMMA lamination. Therefore, plasma bonding was not possible. This led to the utilization of adhesives to bond the outlet to the platform. Unfortunately, the bond with the adhesives was not durable and it easily teared after prolonged experiments in the incubator.

4.5.2 Semi-monolithic PMMA outlets

The complete transition to thermoplastics allowed us to completely redesign the outlet and its fabrication strategy. With the advantage of CO_2 laser cutting, we were able to incorporate the outlet to the well-plate. The design of the outlet is based on a through hole with a diameter of 2.4 mm. Additionally, the design includes a micro-well that is rastered on the top surface of the plate.

The installation process involves inserting a 2.44 mm SILGARD® tubing to the outlet opening and filling the micro-well with Gorilla Superglue ® to ensure a complete seal and hold the tubing in place (Fig. 28a). This method resulted on a very resistant and air-proof outlet, optimal for proper functionality and user handling (Fig. 28b). Additionally, the platform is optically clear and allows the user to observe the flow when the device is operating.

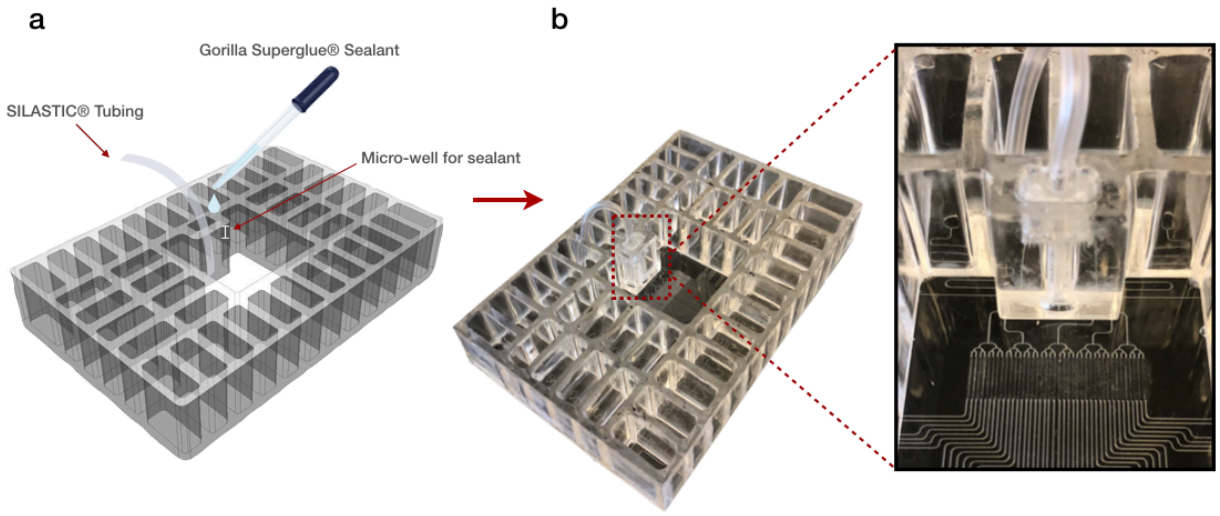

Figure 28 Semi-monolithic PMMA outlet. a) Installation process and details b) Final look

5. Device characterization and functionality

5.1 Quality control - device variability of flow

Each fabricated device follows a quality control protocol to ensure its proper functionality. In this process, we investigate the how uniform the flow is across one device and the variability in its replicates (Fig.29)

Figure 29 Device quality control

The first point of interest is outlining the variability of flow rate within a device; this helps us understand how variable the flow rate is across each channel. This is accomplished by using the device of interest at different flow rates in a controlled time frame. For example, an experiment was performed using one device by filling every well with a measured volume of 10 ml and ran at 1 ml/hr. and 1 ml/hr. for 2 and 16 hours respectively. As shown in Table 11, there was a percent deviation of 11.3 and 10.6 for the 10 ml and 1 ml/hr. flow rate respectively. This information is critical for when this specific device is used in an actual biological experiment. Knowing the variability of the device allows the user to have an idea of how the device needs to be operated. Specifically, when the device would deplete the solutions in each well during a prolonged experiment.

Table 11 Flow rate variability across channels in one device

Start Volume	***Flow Rates***	***Avg. Flow Rate***	***% St. deviation***
1 ml	**10 ml/hr. (2 hrs.)**	266.5 μl/hr.	11.3
1 ml	**1 ml/hr. (16 hrs.)**	27.1 μl/hr.	10.6

The second point of interest in the quality control protocol is understanding the variability across device replicas. We assess the variability across devices by filling them with a measured volume and running them at a controlled flow rate. To illustrate this part of our quality control, we compared three different devices as shown in Table 12. The results demonstrated that there was a difference in variability across devices ranging from ~4% to ~8%. This information indicates how variability of the functionality across each device replica.

Table 12 Flow rate variability across different devices

	Device		
	1	2	3
%St. Dev	8.08	6.71	4.21

This quality control will be followed for every set of devices fabricated in the near future. With this information we intend to have detailed device performance information for when specific device is utilized for experimental assays. We also expect to lower the variability across devices by identifying which step of the fabrication protocol might be contributing to such variations on flow rate.

5.3 Lateral diffusion assessment using fluorescein

In order to establish a complete user protocol to utilize the device for prolonged biological experiments, we had to establish a flow rate that would ensure localized delivery without cross contamination between adjacent channels. The device begins operation when the open channels in the central culture chambers are sealed with a porous PTFE membrane (containing tissues). The PTFE membrane is highly porous and allows for lateral and vertical diffusion.

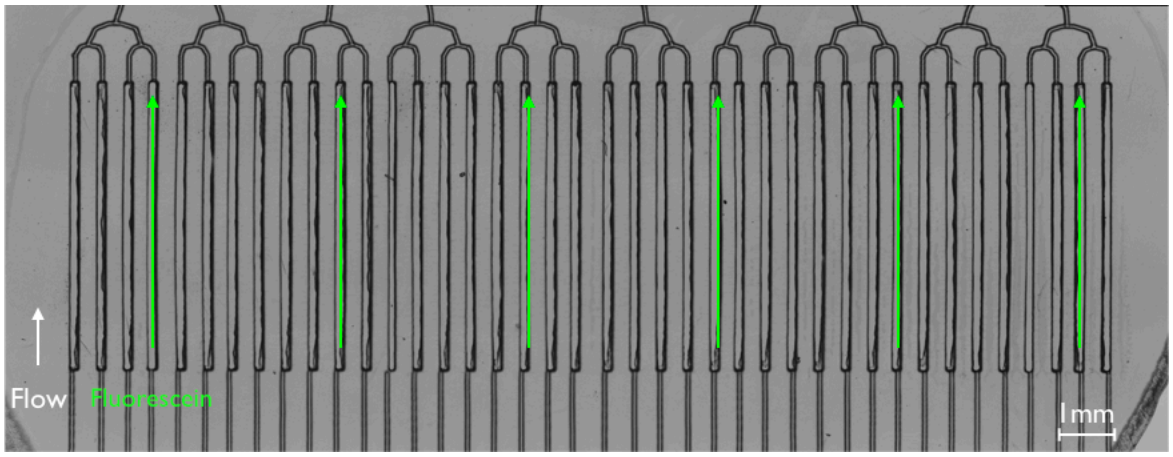

Figure 30 Location of fluorescein delivery channels

To establish the minimal flow rate at which the device can be utilized, we sealed the open channels of the device with a PTFE membrane and ran 100mM fluorescein across 6 of the 40

delivery channels, with the rest having PBS. Each of the 6 delivery channels was separated by 6 channels to analyze spread three channels over on both directions when possible (Fig.30).

After loading the device with fluorescein on the selected channels, it was tested at 0.1 ml/hr, 0.2 ml/hr, 0.3 ml/hr, 0.4 ml/hr, 0.75 ml/hr, 1 ml/hr, and 10 ml/hr. Images were taken at each flow rate after waiting for equilibration for approximately 10 minutes. To have a better understanding of the maximum relative fluorescence of the compound, images were taken at 7ms and 70ms exposures for every condition. After all the images were taken, we performed two quantitative analyses of lateral diffusion up, middle and downstream across the 6 channels of interest (Fig. 31). The first analysis was an overall diffusion with a profile along the delivery channels and its three adjacent channels. The second analysis encompassed a detailed inspection of the relative fluorescence in each of the three channels adjacent to the delivery channel.

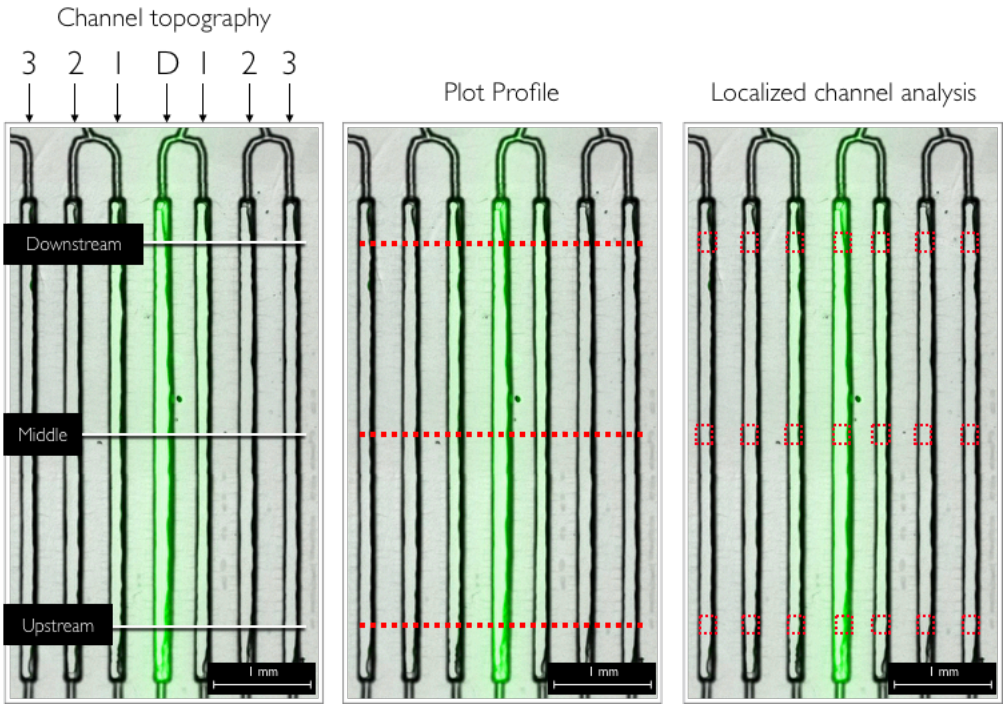

Figure 31 Channel topography and analysis methods performed for each channel containing fluorescein

Through the profile analyses, we were able to have an overview of the lateral diffusion occurring on top of the membrane at 7 different flow rates. As shown in Figure 32, the lateral diffusion increases as the flow rate decreases. Similarly, as expected, the lateral diffusion is higher downstream of the delivery channel compared to the middle and upstream location. From these results we were able to observe how there is minimal fluorescein signal on the first channel adjacent to the delivery channel with flow rates above 0.4 ml/hr. Similarly, the signal two and three channels away from the delivery channel was minimal and barely visible at flow rates above 0.4 ml/hr. Nevertheless, we still required a more detailed assessment of the relative fluorescence at each of the channels of interest.

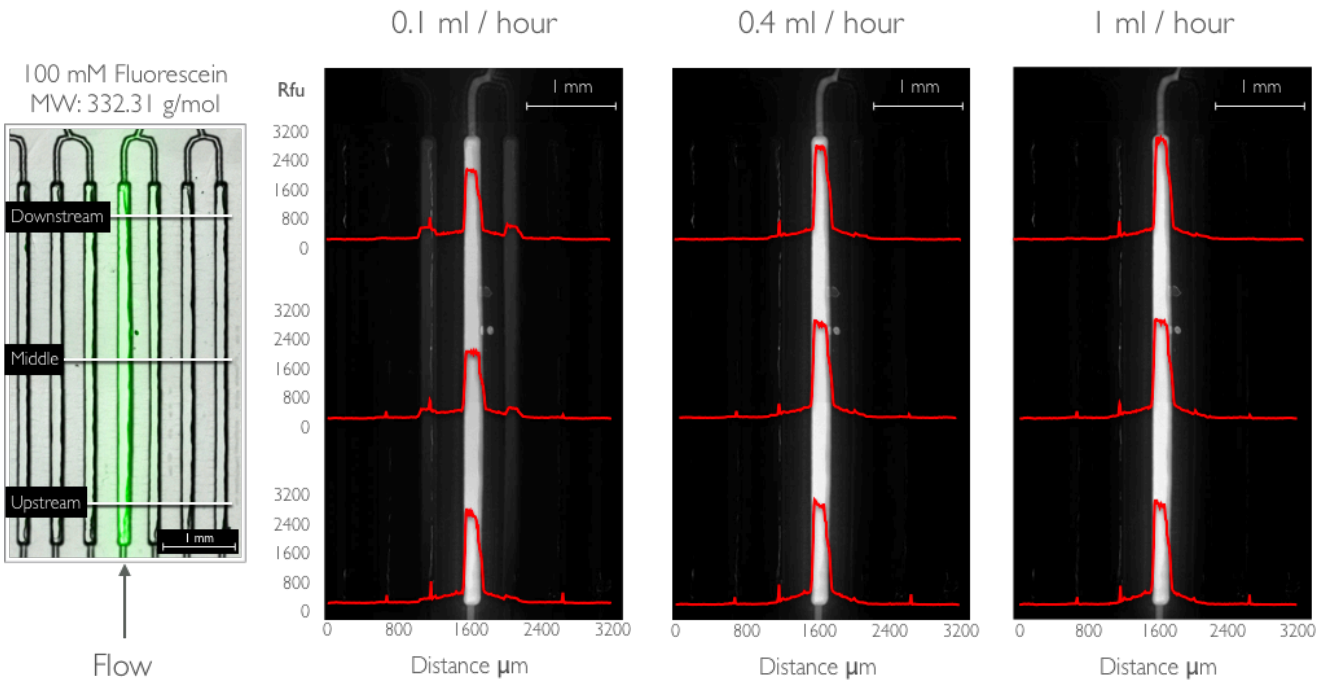

Figure 32 Example of lateral diffusion assessment at one location with different flow rates

To have a better quantification of the spread happening from the delivery channel, 3 regions of interest (upstream, middle, and downstream) were selected at the delivery channel and all of its neighboring channels (3 on each side). By doing so, we were able to get a measure of spread one, two, and three channels away from the delivery channel. The analysis was performed by taking an average of the relative fluorescence at the selected regions for every channel for every condition. First, to have a better approximation, we performed a background subtraction. This was accomplished by selecting an area for every sample that was far from the area of analysis but inside the region with the PTFE membrane. Then we took average an average for the relative background florescence of all the samples. Then the data was pooled and averaged based on the location of the channel (one, two, or three away from the delivery channel). Having the averages, we subtracted the background fluorescence for each sample at both exposures (7 and 70ms). Subsequently, we utilized the overexposed (70 ms) data to obtain a correction factor to match the 7ms with the 70ms data. Knowing that the data at 70ms represented the 100% intensity, we utilized the correction factor to match the over exposed data. Afterwards, the data was combined. In our final analysis, we utilized the adjusted data from the 7 ms for the delivery channels and the data from the 70 ms exposure for the adjacent channels. Finally, we normalized the data with the average fluorescence at the 6 main delivery channels. This analysis was performed for every sample at each of the 7 different flow rates.

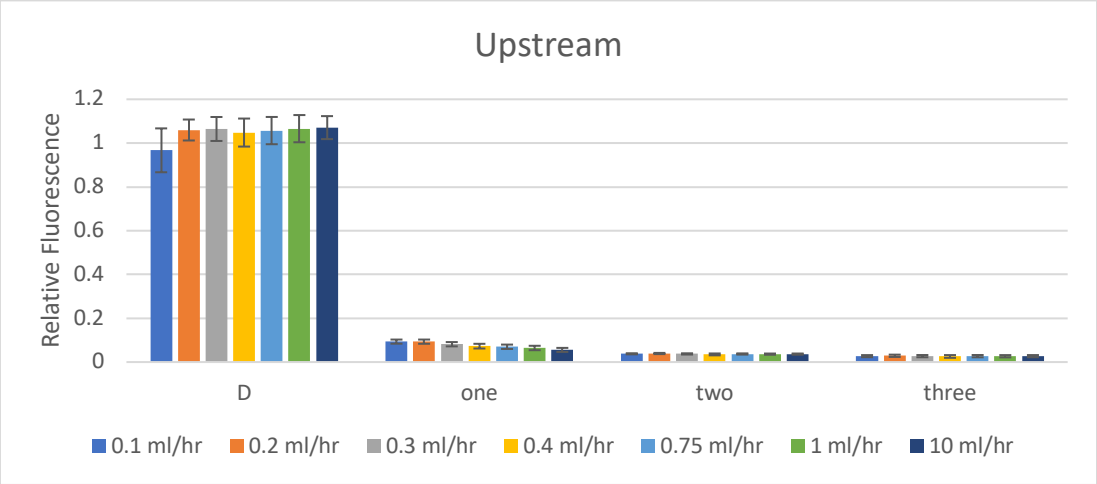

Figure 33 Upstream lateral spread as relative fluorescence one, two, and three channels away from the delivery channel at 7 different flow rates

As shown in Figure 33, there is minimal spread happening upstream of the channels. Starting at 0.1 ml/hr. there is about 10% fluorescence relative to the average fluorescence in the delivery channel. Clearly the fluorescence decreases as the flow rate increases. During an experiment, the channel next to the delivery channel, serves as a sink to prevent further spread to the next channel. Therefore, we are mostly interested in quantifying the spread two and three channels away from the delivery channel.

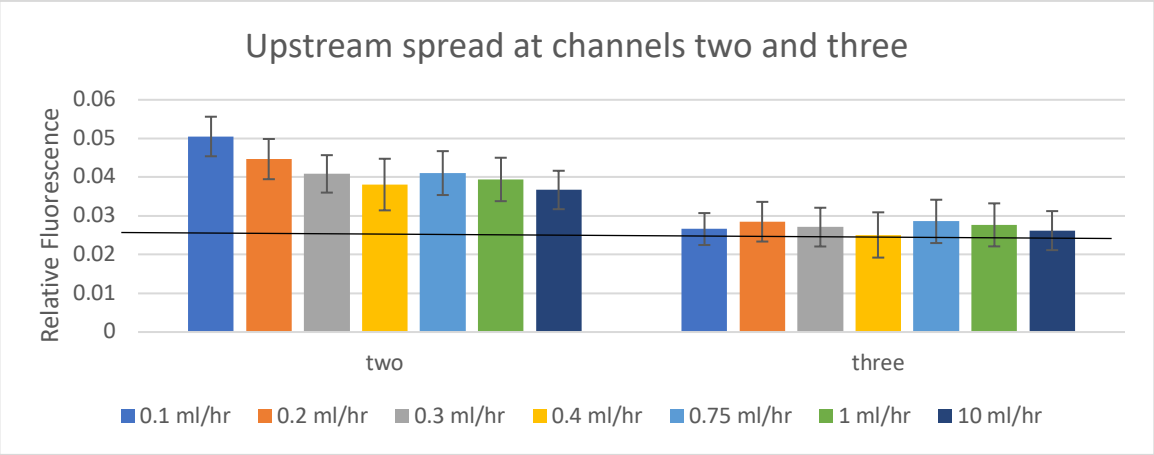

Figure 34 Upstream spread two and three channels away from the delivery channel

Figure 34, shows the spread at two and three channels away from the delivery channel. Knowing that diffusion is lowest upstream of the flow at any given point of the channels, we calculated the average fluorescence at the channel located three channels away from the delivery channel at the highest flow rate and established it as our lowest baseline (black line). This baseline represents the lowest amount of fluorescence observed for all of the samples. With the established baseline, we could determine that there was a ~2% relative fluorescence two channels away for flow rates above 0.4 ml/hr. Similarly, for the channel located three channels

away from the delivery channel, we observed a ~1% at flow rates above 0.4 ml/hr. We performed the same analysis for the middle and downstream locations of the channels (Figs. 35, 36, 37, 38).

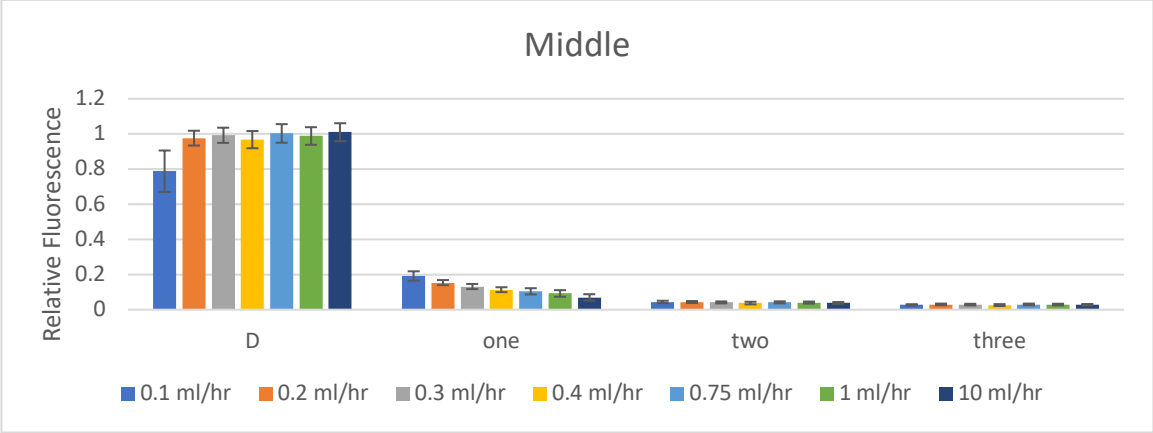

Figure 35 Middle spread as relative fluorescence one, two, and three channels away from the delivery channel at 7 different flow rates

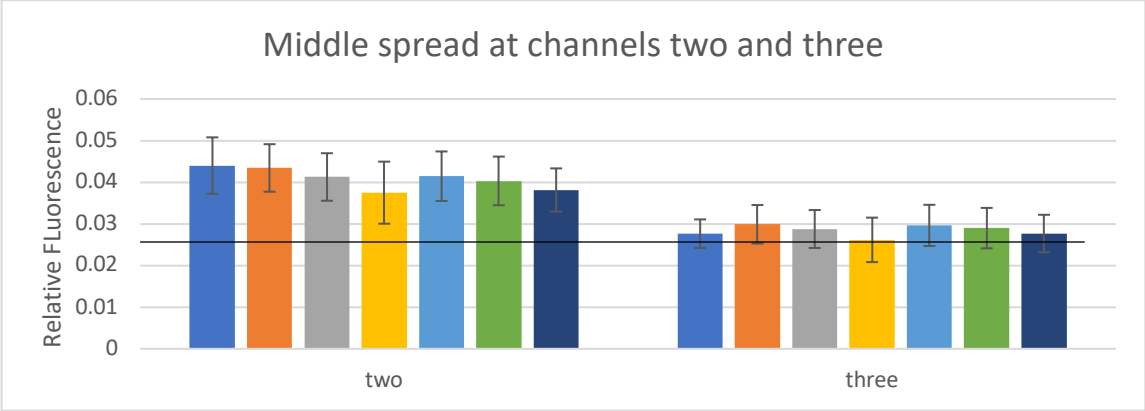

Figure 36 Middle spread at channels two and three away from the delivery channel

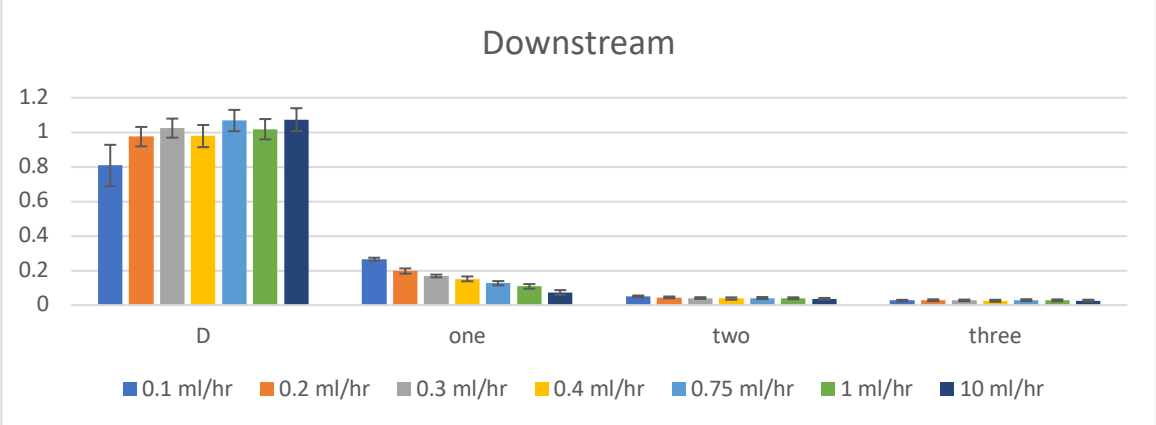

Figure 37 Downstream spread relative fluorescence one, two, and three channels away from the delivery channel at 7 different flow rates

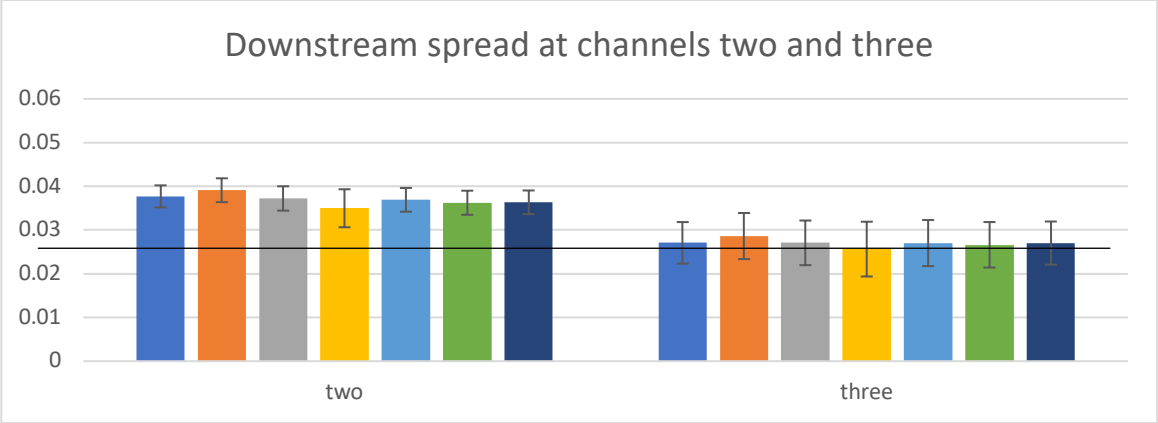

Figure 38 Downstream spread two and three channels away from the delivery channel.

The results obtained after this set of experiments, gave us valuable information regarding the lateral diffusion happening at the surface of the PTFE membrane. With these results we were able to have a better idea of what are the optimal conditions at which the device should be operated during prolonged experimental assays. It is clear for us now that the flow rate at which the device should be utilized needs to be above 0.4 ml/hr. Moreover, when performing drug efficacy analyses, there must be a channel in between delivery channels containing drugs. Therefore, the user could decide to utilize up to 20 of the 40 delivery channels for different drug compounds.

Having an idea of the conditions at which the device should be utilized we could estimate how long could the device be in operation. Knowing that each well can contain up to 1.6 mL and assuming that the device is used at 1 ml/hr. (25 μL/hr./well). and that a 60 ml syringe is utilized in the syringe pump, the device could run without having to be refilled for about 60 hours until the syringe needs to be replaced or emptied. To have a better control and to ensure that the device does not reach complete depletion, we have found that it is best to calculate the time until ~250 μL of solution is left in each well. Therefore, at 1 mL/hr. it would take about 54 hours for 1.35 mL to be depleted from each well. It is important to note that these calculations are based assuming that there is no variability in the flow rate of every channel; in other words, the flow rate is the same for every channel.

From the results obtained in our quality control assessment, we observed that there could be a variability ranging from 4-8%. If we assume that one of the channels is running 8% faster than every other well, we could adjust the calculation to know how long the device could be used before the well that runs faster reaches depletion. Assuming that the device is operated at 1 ml/hr. (25 μL/hr./well), the channel running at the fastest flow rate would run at 27 μL/hr. Therefore, it would take about 50 hours for 1.35 mL to deplete. This demonstrates the importance of building platforms with very low variability. A small variability of 8% means 4 hours less of untouched device operation.

5.2 Fluorescent dye delivery

To demonstrate spatially controlled drug delivery, we delivered three different colors of cell nuclear staining reagents, Hoechst (blue), CellTracker™ Green CMFDA, and CellTracker™ Red CMPTX to an intact U87 tumor slice. (Fig. 39a). Each reagent was separated by a buffer lane with PBS and exposed for 1 hour at 2 ml/hour. As shown in Figure 28a&b, reagents can be selectively delivered to the regions of the tissue slice with minimum lateral diffusion. To demonstrate the penetration depth of reagents into the tissue slice, the slice was sectioned and analyzed with fluorescence microscopy (Fig. 29c&d).

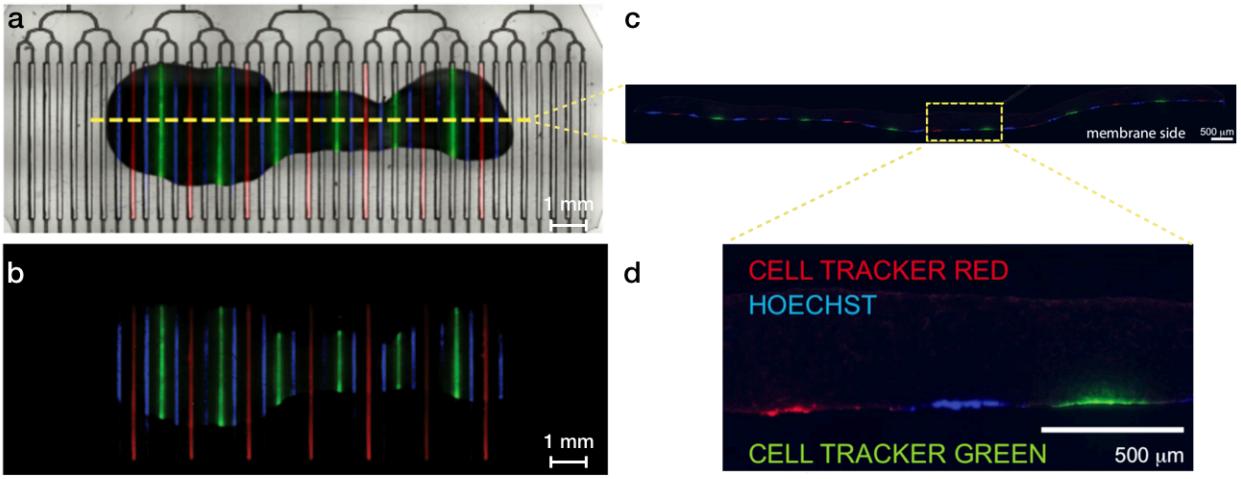

Figure 39 Fluorescent dye delivery a) Composite image to demonstrate cell tracker red, cell tracker green, and Hoechst delivery locations. b) Composite fluorescent image of delivery channels. c) Tissue section after 1 hour of exposure. d) Close up of tissue section to demonstrate tissue perfusion after 1 hour of exposure within the device.

With this experiment we were able to confirm the results of our lateral diffusion assessment. Nevertheless, we still required further analysis of the tissue perfusion (vertical diffusion) happening as a function of time.

5.4 Tissue perfusion assessment with Hoechst and Doxorubicin

In addition to understanding lateral diffusion at the surface of the tissue slice, it was fundamental to demonstrate how compounds of interest in any given experimental assay would diffuse/perfuse into the tissue as a function of time (Fig. 40). In this investigation we selected two fluorescent compounds, Hoechst (blue) and Doxorubicin (red), a common cancer chemotherapy. These compounds were delivered to a live U87 GBM xenograft slice with a thickness of 250µm. The tissue was cultured on a PTFE membrane and transferred to the culture chamber within the device after one day of incubation. The compounds were separated by a buffer lane and arranged in an alternating fashion (Hoechst, buffer, Dox, etc.). To understand tissue perfusion as a function of time, the compounds were added at different time points while the device was in continuous operation; all of the wells were initially filled with slice medium. The tissue was exposed to four different time points, 8, 4, 2, and 1 hour. This was accomplished by just removing the slice

medium and adding the fluorescent compounds to the selected delivery wells at the corresponding time point.

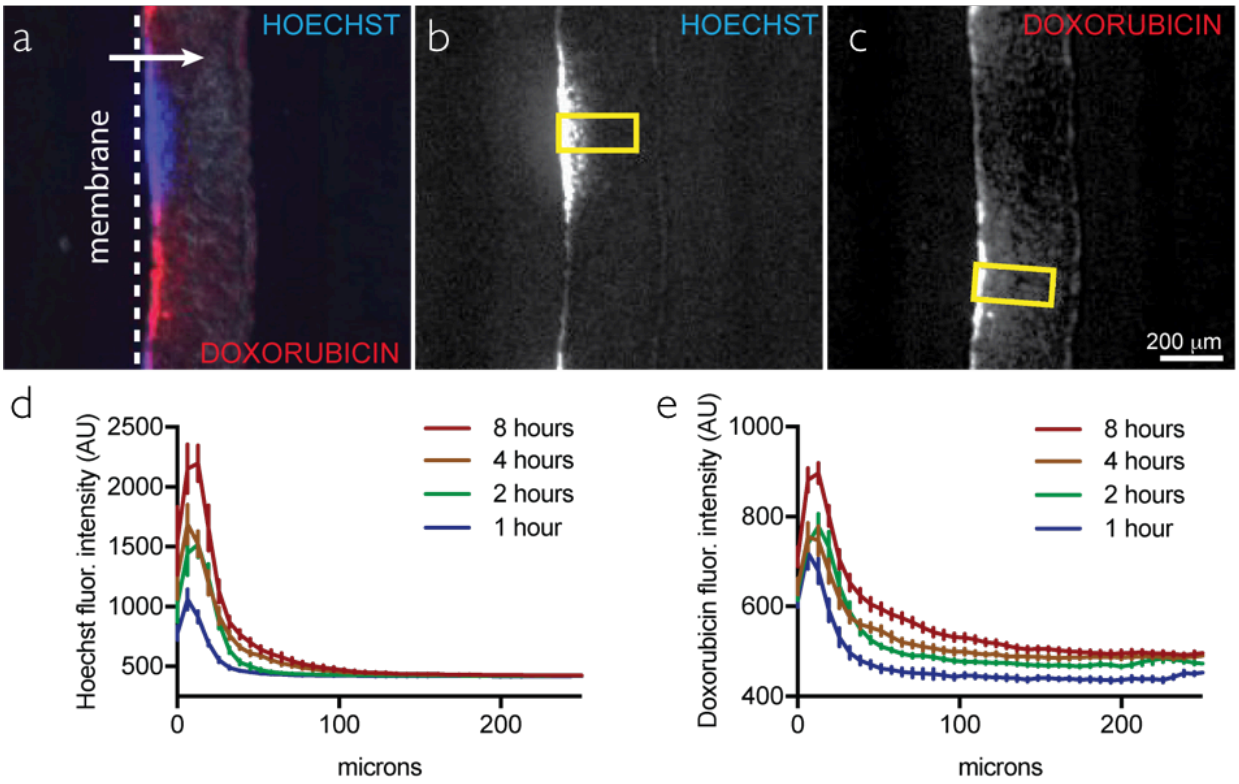

Figure 40 Tissue Perfusion as a function of time. a) Composite fluorescent image of tissue section exposed for 8 hours to Hoechst (blue) and Doxorubicin (red). b) Example of analysis area for tissue perfusion/vertical diffusion of Hoechst after 8 hours of exposure. c) Example of analysis area for tissue perfusion/vertical diffusion of Doxorubicin after 8 hours of exposure. d) Quantification of Hoechst perfusion into tissue after 8 hours of exposure. e) Quantification of Doxorubicin perfusion into tissue after 8 hours of exposure.

Figure 40a, illustrates a tissue section after 8 hours of exposure to Hoechst and Doxorubicin. The membrane side is placed on top of the delivery channels, allowing for vertical diffusion into the tissue (shown from left to right in this figure). To have an idea of the tissue perfusion happening as a function of time, we analyzed the fluorescent signal at the middle of the delivery regions within the tissue section (Figs. 40b&c). The selected area, shown in yellow, was about 100µm x 200 µm. Then, an average fluorescence was taken for every sample at every time point utilizing the same area for analysis.

As expected, results demonstrated that tissue perfusion increased as function of time for both compounds (Figs. 40d&e). Figure 40d, demonstrates tissue perfusion for Hoechst as a function of time. For Hoechst, there was a perfusion of about ~100 µm after 4 hours of exposure and ~120µm after 8 hours of exposure. There was a minimal ~50 µm perfusion after 1 and 2 hours of exposure. On the other hand, as shown in Figure 40e, Doxorubicin had a higher tissue perfusion compared to Hoechst. Although the fluorescent intensity of the compound was lower, the perfusion can be clearly observed by comparing the fluorescence on the neighboring sections of the tissue in Figure 40c.

With the results obtained from this investigation, we were able observe tissue perfusion as a function of time. Moreover, we also learned how much time would a tissue need to be exposed in the platform for complete perfusion. Further studies need to be performed with compounds of different molecular weights to have a better idea of the actual diffusivity constant of the membrane and tissue slice complex. With an approximation of a diffusivity constant a COMSOL model could be built to predict exactly how much time would a tissue need to be exposed a given compounds to achieve maximal perfusion.

6. Experimental assays

The development of more effective cancer therapies still requires better ways to accurately predict drug efficacy in individual patients [10]. Oncoslice enables multiplexed testing of cancer drugs on intact tissue slices and has the potential for personalized medicine by serving as a tool to identify the most effective therapies for individual cancer patients.

To demonstrate this potential, we utilized glioblastoma multiforme (GBM) xenografts as our initial experimental proof of concept. A complete investigation of the GBM model was performed before being utilized in the platform. The investigation entailed a thorough analysis of the xenograft-derived tumor slice assay, including optimal timing for slice culture and conditions to preserve the cellular microenvironment.

The ideal testing workflow, is shown in Figure 41. As the figure illustrates the first 6 steps involve the development of tissue slices. These steps are usually the most challenging of the process, as the optimal conditions for slice culture must be determined for each cancer type. The rest of the protocol involves the application of the device for drug experiments and analytical procedures to determine drug efficiency.

The first set of experiments involved using a previously determined protocol based on a U87 GBM cell line. Having determined the proper slice culture conditions, we tested the performance of the device for multiplexed drug delivery experiments. Two main experiment modalities were performed, a dose response assay with cisplatin and a multiplexed drug delivery with 5 different drugs. A thorough analysis was performed for each experiment and we were able to determine the most effective cisplatin drug concentration and drug, for each experiment respectively.

Following the experiments based on xenografts, we also performed various experiments utilizing patient biopsies. We followed the same workflow shown in Figure 41, with the exception of the animal model; for these experiments a patient biopsy was sectioned and cultured prior to experimentation. We were able to perform drug efficacy experiments with metastatic colorectal cancer samples obtained from Dr. Raymond Yeung at UW medicine. Dr. Yeung, provided our lab with samples of patients that have been already exposed to various chemotherapies. With our platform we were hoping to obtain more information on the possible acquired drug resistance of the patient by exposing a limited number of intact tissues to a different set of drugs.

Through these assays we hope to further demonstrate the capabilities of the platform. We hope that with our device, we can streamline the identification of drugs that are the most effective for the treatment of a cancer patient's solid tumor by observing cancer cell death when exposed to a panel of drug candidates. Most importantly we believe this technology could provide a key missing link between drug testing in cell or animal models, and testing in actual human cancer tissue. This new method will allow for testing treatment efficacy on the patient's own tumor tissue in a timeline that allows for the results to influence a patient's therapeutic strategy.

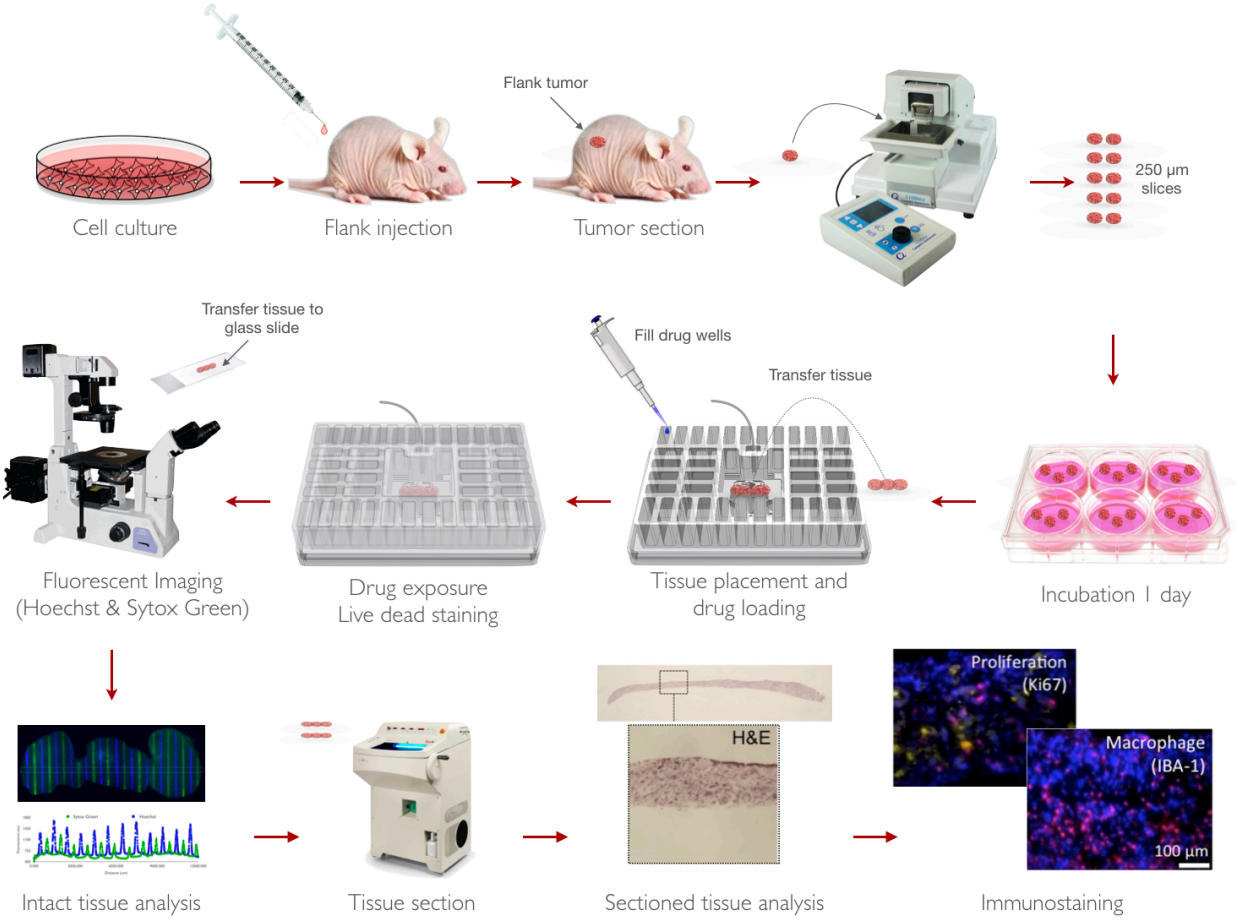

Figure 41 Device workflow overview

6. 1 U87 Mouse Xenografts

At the Folch lab, an extensive investigation was performed to define the optimal biological parameters of the GBM U87 slice culture model and to determine the relevant the timing for drug delivery and analysis. This investigation defined the slice assay conditions, including optimal timing for slice culture and conditions to preserve the cellular microenvironment.

With the results of this investigation we employed the ideal slice culture conditions to perform drug exposure experiments utilizing the microfluidic platform. U87MG cells (ATCC) were grown

in DMEM/F12 (Invitrogen) supplemented with 10% fetal bovine serum and penicillin/ streptomycin. Cells were passaged every 3-5 days at ~70% confluency. Mice were handled in accordance with a protocol approved by the University of Washington Animal Care and Use Committee. Male immunodeficient nude mice (Taconic, Foxn1 nu) aged 4-10 weeks were injected subcutaneously in the flank (~1 million cells in 200 μL of serum and antibiotic free medium). Mice with flank tumors were sacrificed before tumor volume reached 2 cm (2-4 weeks). Once sacrificed, tumors were removed, and 250 micron-thick slices were cut with a 5100mz vibratome (Lafayette Instrument) and cultured on top of PFTE 0.4 um transwell membranes (Millipore) in 6-well plates. The slice culture medium underneath contained Neurobasal-A medium (Invitrogen) with 25% heat-inactivated horse serum (Sigma), Glutamax (Invitrogen), 2x penicillin/streptomycin (Invitrogen), and growth factors (EGF 20 ng/ml and FGF 20 ng/ml, Preprotech or Invitrogen). Medium was changed three times per week. One to two hours before the end of the experiment, nuclear dyes were added to the growth medium: Hoechst (Invitrogen, 10 μM) and Sytox green (Invitrogen 0.5 μM). Then slices were washed three times with PBS for 5 minutes at room temperature. Slices were fixed with 4% paraformaldehyde overnight, then cryoprotected with two changes of 30% sucrose/PBS.

6.1.2 Dose Response to Cisplatin

We utilized the Oncoslice platform to perform a drug response using cisplatin. By following the workflow in Figure 41, we exposed U87 flank tumor slices to Cisplatin with a concentration ranging from 0 to 100μM. After one day in culture on membrane inserts, the tumor and the membrane underneath were transferred to the device.

Multiple tumor slices were lined up to better utilize the drug application window of the device (Fig. 42a). Each concentration of cisplatin was separated by a buffer lane to prevent any possible cross-talk between the different Cisplatin concentrations and to isolate the effect of each concentration.

We applied five different concentrations for 2 days, with 3 repeats per condition, at 2 ml/hour. To mark the locations of drug application, Hoechst dye (1X) was applied in the drug lanes for 2 hours at the end of drug treatment. The tissue was then transferred to a cell culture plate and cell death over the entire tissue was assayed with a Sytox Green (1x) treatment (Fig. 42b&c); localized drug application led to variable cell death.

As expected, the device showed similar results compared to the tissues exposed off the device (Fig 42d&e); a large amount of cell death was apparent on concentrations above 10μM Cisplatin on and off the device. A one-way ANOVA was performed for both off device and on device drug exposures. Results indicated a significant difference in response for Cisplatin concentrations of 30μM and 100μM for both experiments (off and on device). There was also a slight response of low concentrations of cisplatin in the tissue exposed on the device. We believe that this is possible to a strong effect of the higher concentrations of cisplatin in nearby locations.

This experiment demonstrated the capability of the platform to perform drug response experiments on patient samples. Having the ability to determine the optimal drug concentration for a specific treatment and patient is critical, specifically when a new drug is in its developmental stages.

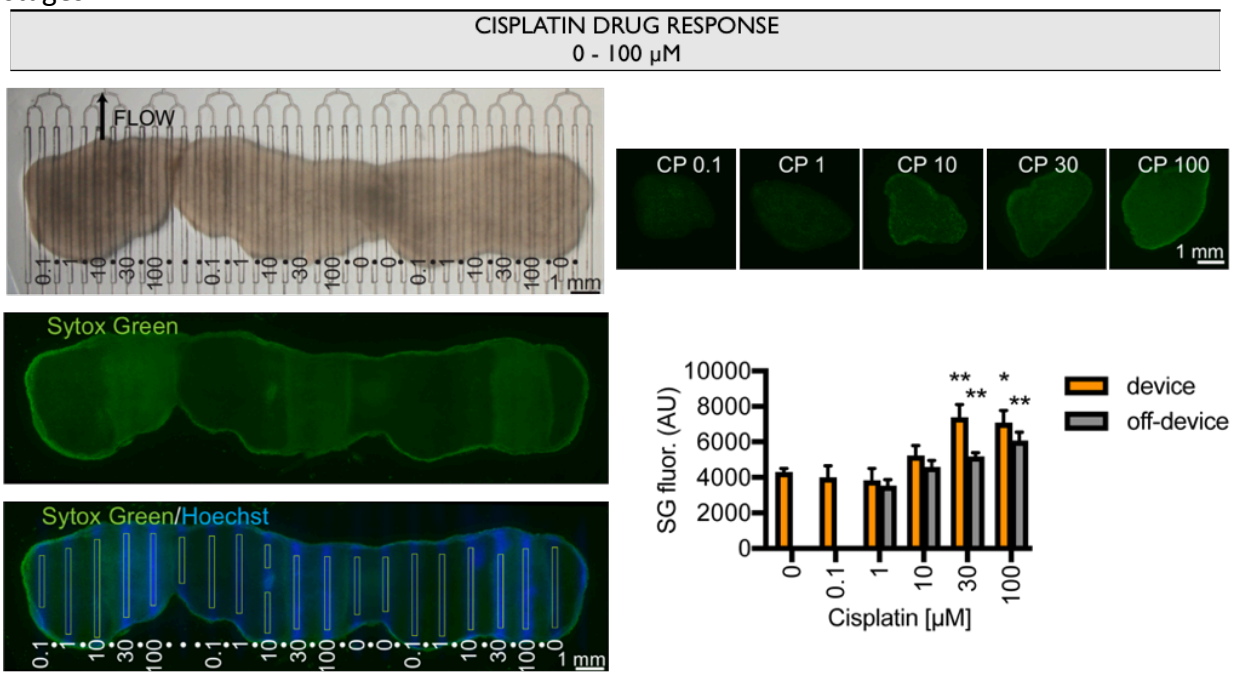

Figure 42 Cisplatin drug response

6.1.3 Multiplexed Drug Delivery

After performing a drug response experiment with the device, we decided to use the device to test a panel of 4 different drugs: cisplatin, bortezomib, mocetinostat, and parthenalide (Fig 43). As with the drug response assay, multiple U87 flank tumor slices were lined up to better utilize the drug application window of the device (Fig. 43a). A total of three lanes were utilized for each condition with intervening buffer lanes to prevent crosstalk between each compound. The tissues were exposed for 2 days at 2 ml/hour.

At the end of the experiment Hoechst dye was run in the drug lanes for 2 hours to localize drug application. Afterwards, to analyze cell death, the tissue was transferred to a cell culture dish and exposed to Sytox Green. Localized drug application led to variable cell death, as seen in figures 43 b and c. To compare drug response off the device, 3 slices per condition were cultured and exposed concurrently on a 6 well plate, followed by an exposure to Sytox Green (Fig. 43d).

As shown in Figure 31e, the response on and off the device were very similar. Large amounts of cell death were apparent with Parthenolide and Cisplatin, while smaller amounts were seen with Mocetinostat and limited cell death with Bortezomib. A one-way ANOVA was performed for both off device and on device drug exposures. Results confirmed a significant response for Parthenalide, Cisplatin, and Mocetinostat for the device experiment.

With this experiment we intended to demonstrate the ability of the platform to perform spatially controlled drug exposures utilizing different therapies. By expanding these experiments to human samples, we hope that our platform could be used as a tool that accurately predicts drug efficacy in individual patients.

DRUG PANEL		
C Cisplatin 100µM	B Bortezomib 1µM	M Mocetinostat 30µM
P Parthenolide 200µM	D DMSO 0.2 %	• Buffer

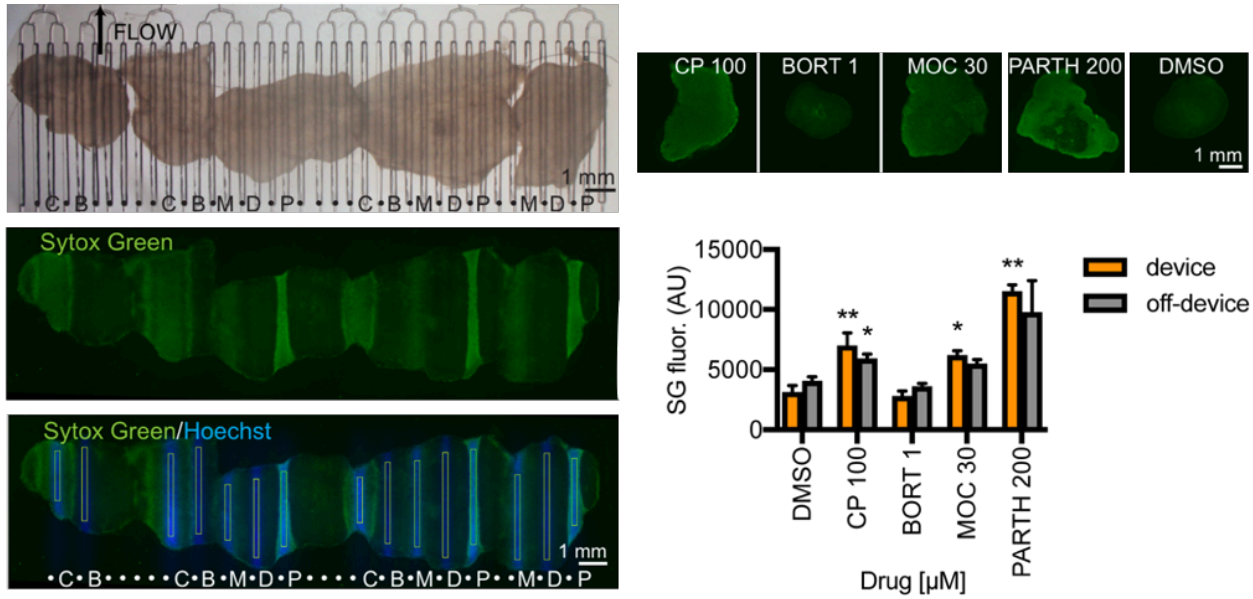

Figure 43 Multiplexed drug delivery

Apart from demonstrating the effect of the different drugs at the surface of the tissue, we also analyzed the effect of the drugs inside the tissue. The sample tissue was sectioned and immunostained with cleaved caspase 3 (CC3) to investigate apoptosis in the regions exposed to the different drug compounds (Fig.44a). This analysis gave us a better idea of the efficiency of each drug after the 48 hours of exposure.

As shown in Figure 44b, the areas of the tissue exposed to the drugs show varying amounts of apoptosis within the tissue. The areas exposed to cisplatin and mocetinostat had the higher apoptosis, followed by parthenalide and bortezomib respectively. This analysis also demonstrated the differential response on the surface and within the tissue. The results obtained for the cell death analysis at the surface of the tissue indicated that parthenalide had the highest response, followed by cisplatin and mocetinostat respectively. Additionally, it further demonstrates the capability of the platform for selective drug delivery. The separation of each drug with a buffer lane, isolated the effect of the different compounds of interest.

Through this experiment we were able demonstrate a complete representation of an experimental assay with the platform. This protocol can also be expanded to analyze other relevant factors related to drug efficacy, such as proliferation with Ki67 or to investigate the presence of other cell types to assess the tumor microenvironment. In the near future we expect to utilize this protocol for other cancer types and actual human samples.

DRUG PANEL		
C Cisplatin 100μM	B Bortezomib 1μM	M Mocetinostat 30μM
P Parthenolide 200μM	D DMSO 0.2 %	• Buffer

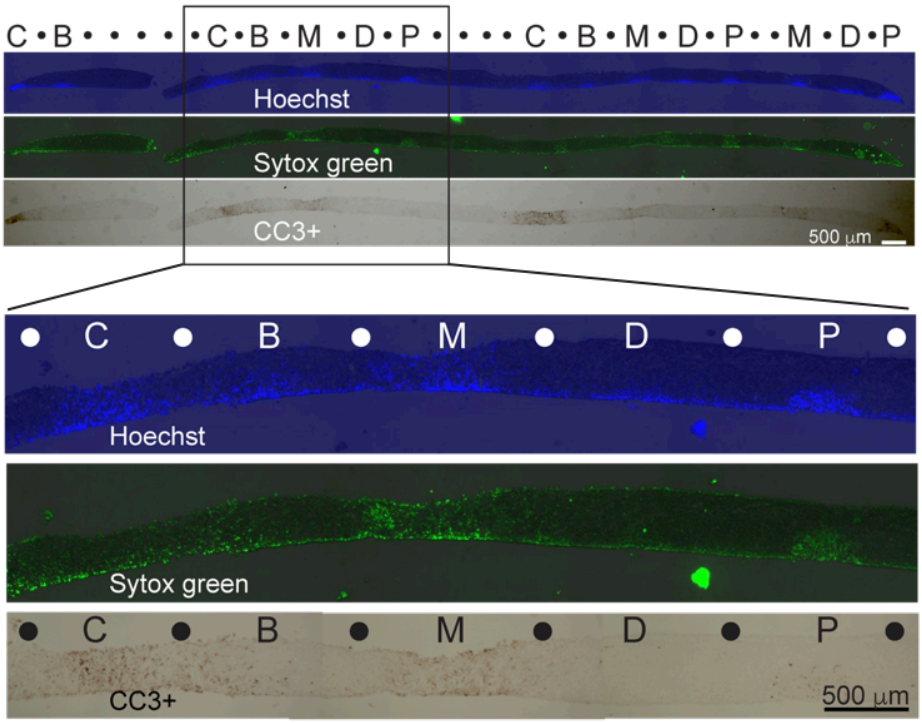

Figure 44 Tissue sections of exposed U87 tumor slice.

6.2 Human Samples - Colorectal Metastatic Cancer

The experiments performed with U87 GBM mouse xenografts gave us a clear idea of the functionality of our platform and the ideal conditions to achieve the best performance. The results motivated us to expand our studies the application of our device to human samples, which is the main goal of the project. In order to get tumor samples, we contacted Dr. Raymond Yeung at UW Medicine. Dr. Yeung is a UW professor of Surgery and adjunct professor of Pathology. His clinical focus is on the surgical treatment of tumors of the liver and bile duct and metastatic disease involving the liver. Within his group, Dr. Heidi Kenerson focuses on assessing drug efficacy on tumor slices obtained from core biopsies of patients with liver cancer and other metastatic tumors. Additionally, Dr. Kenerson characterizes the viability of each tumor slices and has been investigating the ideal culture conditions for the human derived tumor slices.

Prior to exposing tissue slices, the viability of tumor slices is analyzed through an MTS cell proliferation assay. The MTS assay is based on the reduction of the MTS tetrazolium compound by viable cells to generate a colored formazan dye that is soluble in cell culture media. This conversion is thought to be carried out by NAD(P)H-dependent dehydrogenase enzymes in metabolically active cells. The formazan dye is quantified by measuring the absorbance at 490-500 nm. The viability of the tissue is directly correlated to the absorbance; the higher the absorbance the higher the viability.

We decided to test a set of tumor slices derived from a patient from Dr. Yeung's laboratory. The tumor was a liver metastasis from colorectal cancer. A sample was obtained from a core biopsy, which was sectioned to ~250 μm slices with a vibratome. The tumor slices were cultured for 3 days, assayed for viability, and then prepared for the drug exposure experiment. Three different drug compounds were selected for this experimental assay, Staurosporine, Folfox, and Folfiri, all of which are utilized for colorectal cancer treatment. Staurosporine at 10mM had shown to have a very strong effect in the tumor slices, so it was used as our positive control, while DMSO 6.3% was utilized as our vehicle and negative control as with our other experiments. For this experiment, Folfox and Folfiri were the drugs of interest. It is important to note that the patient had already been treated with both Folfox and Folfiri before the core biopsy was taken.

DRUG PANEL		
S Staurosporine 10mM	X Folfox 1μg/mL	I Folfiri 1μg/mL
D DMSO 6.3%	• Buffer	

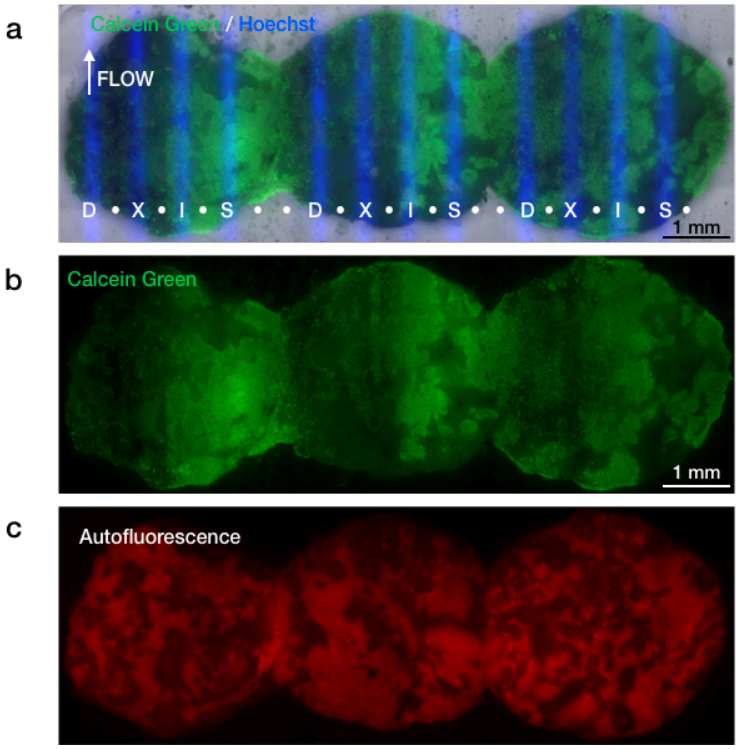

Figure 45 Multidrug exposure of human colorectal cancer biopsy

The drug arrangement of the drug delivery channels is shown in Figure 45a. Each of the compounds of interest was separated by a buffer lane, denoted by a dot symbol. The tumor slices were exposed for 3 days at a flow rate of 2 ml/hr. After exposure, Hoechst was placed on the drug delivery channels for 2 hours to mark the areas of the tissue that were exposed to drugs (Fig. 45a). After labeling the tissue with Hoechst, we analyzed viability with Calcein Green (Fig. 45b).

Unfortunately, we were not able to perform an assessment of drug efficacy on the surface of this tumor sample, mainly due to the heterogeneity of the tissue. There was a significant amount of

autofluorescence in what appears to be non-cancer areas around the tissue slices (Fig. 45c). As a result, we were not able to establish a baseline viability for this tissue sample. Additional viability staining with ethidium homodimer and Sytox green was performed, but it was still difficult to clearly assess the viability of the tissue. Due to the heterogeneity of the surface of this tumor sample we are expecting better results through a histological assessment for apoptosis (CC3), proliferation (Ki67). Similarly, through Haemotoxylin and Eosin staining we expect to better assess the tumor slice heterogeneity. Although we were not able to obtain good results pertaining the efficacy of the drugs of interest on the surface of the tumor slices, we gathered valuable information regarding the areas of our protocol that require improvement for better analysis. We expect to continue receiving human tumor slices from Dr. Yeung's laboratory and to improve our testing methods.

7. Conclusions and Future Work

In this project we were able to develop a redesigned architecture of Oncoslice and a new fabrication protocol based on digital manufacturing techniques which will hopefully enable our platfrom to serve as a tool for drug development and personalized medicine. The challenges that came with the first platform design motivated us to perform a complete architecture redesign and a thorough investigation of potential manufacturing techniques compatible with large scale manufacturing. Through this project, we were able to gain a better understanding of microfluidic device fabrication based on thermoplastics and the associated bonding techniques commonly used in the field. By carefully assesing techniques such as CO_2 laser for fabrication and bonding techniques such as thermal fusion bonding, indirect transfer adhesive bonding, direct solvent bonding, and lamination, we were able to determine which were best for the characteristics and dimensions of our platform.

With the improved fabrication protocol, we were able to reduce the time of fabrication from ~4 days to ~2 hours. Apart from reducing the fabrication time, we were able to develop a protocol that does not require a highly skilled lab technician. Compared to photolithography and soft-lithography fabrication techniques, which require training and aquired experience, the digital manufacturing techniques of our new protocol would only require utilizing a set of CAD files and following instructions for processing and assembly. The simplicity of our fabrication protocol allows for any person witihn our lab to develop this device within a week of training.

Although we were able to greatly reduce the fabrication time of the platform, there is still room for improvement. One key step that needs to be improved is the fabrication and processing of the 40 well-plate. Currently, the 40 well-plate takes about 50% of the total fabircation time. This is mainly due to the time it takes to laser cut and to flatten. We believe this time can still be optimized by improving the step-wise laser cutting technique and by reducing the time employed for surface flattening.

In adddition to an improved fabrication protocol, we were able to determine the optimal operating conditions of our platform for experimental assays. Through an evaluation of lateral and vertical diffusion we were able to characterize the ideal flow rates at which the device should be utilized. Similarly, we were able to approximate tissue perfusion over time. With this information, any given user would have a better idea of how to utilize our platform and how long would tissue samples need to be exposed to ensure tissue perfusion. Additional studies still need to be made to have a better estimate of tissue perfusion based on the molecular weight of any given compound.

With our redesigned platform we were also able to demonstrate its potiential through experimental assays utilizing mouse xenografts and human tumor samples. With the mouse xenograft model, we were able to perform dose response and mutli drug response experiments. Our results clearly demonstrated the spatial control that can be achieved with our platform. For the dose response experiment with Cisplatin, we were able to show a range of concentrations

that would be the most efficient for the U87 GBM xenograft samples. Similalry, we were able to show a differential response through a multi-drug experiment. Finally, we were also able to begin the application of our platform to assess drug efficacy in human samples. In our first experiment with tumor slices derived from a liver metastsis of colorectal cancer, we were able to gain a valuable insight on areas that need to be improved for data analysis. Future work would focus on establishing an improved pre and post tumor slice processing protocol for viability and tumor microenvironment assessments.

In the nearest future we plan to continue experimental assays with both mouse xenografts of other cancer types and human samples. We expect to continue identfying areas of improvement, which ultimately will lead us to a final device design. The first improvement will be focused on the central tissue culture chamber. Currently the PTFE membrane containing the tissue sample needs to be carefully cut from the tissue culture insert and placed on top of the open delivery channels. We plan to redesign the culture chamber to make it compatible with conventional tissue culture inserts. This would greatly improve the user experience by facilitating its operation.

As we advance towards a final design, we expect to transition to injection molding. We envision an injection molded 40 well-plate with a clear bottom. The bottom then have the channel network engraved with the CO_2 laser and sealed with thermal fusion bonding. This process would reduce the fabrication time to approximately ~30 minutes and further facilitate the manufacturing of Oncoslice. We are eager to utilize Oncoslice to further work in the improvement and application of our device in diverse cancer research applications. Our platform has the potential to enable new discoveries in cancer cell biology and facilitate the analysis of the effectiveness of combinations of therapies. The results shown in this manuscript demonstrate the continuous evolution of the platform and its potential to serve as a tool for drug development and the advancement of personalized medicine.

8. References

[1] N. C. Institute, “Cancer Statistics,” *Cancer Statistics*, 2017. [Online]. Available: https://www.cancer.gov/about-cancer/understanding/statistics.

[2] R. Siegel, K. D. Miller, and J. Ahmedin, “Cáncer Statistics,” *Ca Cáncer J.*, vol. 67, no. 1, pp. 7–30, 2017.

[3] NIH, “National Cancer Institute,” 2018. [Online]. Available: https://www.cancer.gov/about-cancer. [Accessed: 05-Jan-2018].

[4] M. Herper, “The Truly Staggering Cost Of Inventing New Drugs,” 2012. .

[5] V. Prasad and S. Mailankody, “Research and development spending to bring a single cancer drug to market and revenues after approval,” *JAMA Intern. Med.*, vol. 10065, p. , 2017.

[6] M. Siddiqui and S. V. Rajkumar, “The high cost of cancer drugs and what we can do about it,” *Mayo Clin. Proc.*, vol. 87, no. 10, pp. 935–943, 2012.

[7] R. K. Harrison, “Phase II and phase III failures: 2013–2015,” *Nat. Rev. Drug Discov.*, vol. 15, no. 12, pp. 817–818, 2016.

[8] BIO industry analysis, “Clinical development success rates 2006-2015,” *Bio Ind. Anal. Rep.*, no. June, p. https://www.bio.org/sites/default/files/Clinical%2, 2016.

[9] N. Shanks, R. Greek, and J. Greek, “Are animal models predictive for humans?,” *Philos. Ethics, Humanit. Med.*, vol. 4, no. 1, pp. 1–20, 2009.

[10] S. H. Shin, A. M. Bode, and Z. Dong, “Addressing the challenges of applying precision oncology,” *npj Precis. Oncol.*, vol. 1, no. 1, p. 28, 2017.

[11] D. Hanahan and R. A. Weinberg, “Hallmarks of cancer: The next generation,” *Cell*, vol. 144, no. 5, pp. 646–674, 2011.

[12] M. R. Junttila and F. J. de Sauvage, “Influence of tumour micro-environment heterogeneity on therapeutic response,” *Nature*, vol. 501, no. 7467, pp. 346–354, 2013.

[13] L. A. Baker *et al.*, “Modeling pancreatic cancer with organoids,” vol. 2, no. 4, pp. 176–190, 2017.

[14] S. F. Boj *et al.*, “Organoid models of human and mouse ductal pancreatic cancer,” *Cell*, vol. 160, no. 1–2, pp. 324–338, 2015.

[15] H. Clevers, “Modeling Development and Disease with Organoids,” *Cell*, vol. 165, no. 7, pp. 1586–1597, 2016.

[16] D. Gao *et al.*, “Organoid cultures derived from patients with advanced prostate cancer,” *Cell*, vol. 159, no. 1, pp. 176–187, 2014.

[17] L. Huang *et al.*, “Ductal pancreatic cancer modeling and drug screening using human pluripotent stem cell– and patient-derived tumor organoids,” *Nat. Med.*, vol. 21, no. 11, pp. 1364–1371, 2015.

[18] C. E. Nash *et al.*, “Development and characterisation of a 3D multi-cellular in vitro model of normal human breast: a tool for cancer initiation studies.,” *Oncotarget*, vol. 6, no. 15, pp. 13731–41, 2015.

[19] C. Pauli *et al.*, “Personalized in vitro and in vivo cancer models to guide precision medicine,” *Cancer Discov.*, vol. 7, no. 5, pp. 462–477, 2017.

[20] M. Astolfi *et al.*, “Micro-dissected tumor tissues on chip: an ex vivo method for drug

testing and personalized therapy," *Lab Chip*, vol. 16, no. 2, pp. 312–325, 2016.
[21] H. L. Haas, B. Schaerer, and M. Vosmansky, "A simple perfusion chamber for the study of nervous tissue slices in vitro," *J. Neurosci. Methods*, vol. 1, no. 4, pp. 323–325, 1979.
[22] O. Jonas *et al.*, "An implantable microdevice to perform high-throughput in vivo drug sensitivity testing in tumors," *Sci. Transl. Med.*, vol. 7, no. 284, p. 284ra57-284ra57, 2015.
[23] R. A. Klinghoffer *et al.*, "A technology platform to assess multiple cancer agents simultaneously within a patient's tumor," *Sci. Transl. Med.*, vol. 7, no. 284, p. 284ra58-284ra58, 2015.
[24] T. C. Chang, A. M. Mikheev, W. Huynh, R. J. Monnat, R. C. Rostomily, and A. Folch, "Parallel microfluidic chemosensitivity testing on individual slice cultures.," *Lab Chip*, vol. 14, no. 23, pp. 4540–51, 2014.
[25] A. Folch, R. J. Monnat, T. C. Chang, L. Horowitz, C. Sip, and R. C. Rostomily, "Microfluidic assay apparatus and methods of use," US 2014/0113838 A1.
[26] M. J. Fuerstman, A. Lai, M. E. Thurlow, S. S. Shevkoplyas, H. A. Stone, and G. M. Whitesides, "The pressure drop along rectangular microchannels containing bubbles," *Lab Chip*, vol. 7, no. 11, p. 1479, 2007.
[27] M. I. Mohammed *et al.*, "Improved Manufacturing Quality and Bonding of Laser Machined Microfluidic Systems," *Procedia Technol.*, vol. 20, no. July, pp. 219–224, 2015.
[28] H. Klank, J. P. Kutter, and O. Geschke, "CO2-laser micromachining and back-end processing for rapid production of PMMA-based microfluidic systems," *Lab Chip*, vol. 2, no. 4, p. 242, 2002.
[29] U. Systems, "Universal Systems VLS3.60." [Online]. Available: https://www.ulsinc.com/products/platforms/vls3-60.
[30] U. Sytems, "Universal Systems ILS 12.50." [Online]. Available: https://www.ulsinc.com/products/platforms/ils1275.
[31] I. R. G. Ogilvie, V. J. Sieben, C. F. A. Floquet, R. Zmijan, M. C. Mowlem, and H. Morgan, "Reduction of surface roughness for optical quality microfluidic devices in PMMA and COC," *J. Micromechanics Microengineering*, vol. 20, no. 6, 2010.
[32] C. W. Tsao and D. L. DeVoe, "Bonding of thermoplastic polymer microfluidics," *Microfluid. Nanofluidics*, vol. 6, no. 1, pp. 1–16, 2009.
[33] S. A. M. Shaegh *et al.*, "Rapid prototyping of whole-thermoplastic microfluidics with built-in microvalves using laser ablation and thermal fusion bonding," *Sensors Actuators, B Chem.*, vol. 255, pp. 100–109, 2018.
[34] T. Data, "Silicone / Acrylic Double Coated Tape," no. mm, 2015.
[35] T. Data, "Adhesive Transfer Tapes with Adhesive 200," pp. 1–4, 2002.
[36] B. L. Thompson, Y. Ouyang, G. R. M. Duarte, E. Carrilho, S. T. Krauss, and J. P. Landers, "Inexpensive, rapid prototyping of microfluidic devices using overhead transparencies and a laser print, cut and laminate fabrication method," *Nat. Protoc.*, vol. 10, no. 6, pp. 875–886, 2015.
[37] S. P. Ng, F. E. Wiria, and N. B. Tay, "Low Distortion Solvent Bonding of Microfluidic Chips," *Procedia Eng.*, vol. 141, pp. 130–137, 2016.